의학박사 학위논문

Development of Micelle-encapsulated ESIONs as a T1 Contrast Imaging Agent

: Prolonged Blood Circulation and Enhanced Hepatobiliary Excretion

T1 MRI 조영제로서 마이셀 캡슐화 ESIONs의 개발 : 혈액 내 순환 연장 및 간 담즙 배설 향상

2020 년 08 월

서울대학교 융합과학기술대학원
분자의학 및 바이오제약학과

서 민 석

의학박사 학위논문

T1 MRI 조영제로서 마이셀 캡슐화 ESIONs의 개발 : 혈액 내 순환 연장 및 간 담즙 배설 향상

Development of Micelle-encapsulated ESIONs as a T1 Contrast Imaging Agent

: Prolonged Blood Circulation and Enhanced Hepatobiliary Excretion

2020 August

Minseok Suh

Department of Molecular Medicine and Biopharmaceutical Science

The Graduate School of Convergence Science and Technology,

Seoul National University

Abstract

Development of Micelle-encapsulated ESIONs as a T1 Contrast Imaging Agent

: Prolonged Blood Circulation and Enhanced Hepatobiliary Excretion

Minseok Suh

Department of Molecular Medicine and Biopharmaceutical Science,
The Graduate School of Convergence Science and Technology,
Seoul National University

Due to clinical concerns about gadolinium toxicity, there is growing interest in the development of alternative contrast agents for magnetic resonance imaging (MRI). Recently, extremely small-sized iron oxide nanoparticles (ESIONs) are attracting considerable attention as a biocompatible T1 contrast agent, which can overcome inherent limitations of conventional T2 contrast agents based on iron oxide nanoparticles (IONPs). Still, there is a lack of studies regarding the actual fate of this novel ESIONs when administered in vivo, which is essential for further clinical translation.

In this study, in vivo biodistribution and pharmacokinetics of micelle encapsulated ESIONs were demonstrated after radiolabeling. Furthermore, using

simultaneous positron emission tomography (PET) /MRI, dynamic change of PET derived radioactivity and MRI signal intensity was directly compared at the same time point.

Micelle encapsulated ESIONs can be an efficient T1 contrast agent with fair r_1 relaxivity of 3.43 mM^{-1}s^{-1} and a low r_2/r_1 ratio of 5.36. Radiolabeling process did not significantly affect the characteristics of the micelle encapsulated ESIONs. In vitro and in vivo stability test revealed that radioactivity of ^{64}Cu well reflects the in vivo dynamics of micelle encapsulated ESIONs. Biphasic blood clearance was observed from the biodistribution study, showing relatively long blood circulation time of 62 min at the distribution phase and 12.8 hours at a elimination phase. As the radioactivity in the blood pool decreased, uptake in the liver increased, and after reaching a peak within 4 hours, it gradually decreased. Up to 40% of administered radiolabeled ESIONs were eliminated through the hepatobiliary system within 24 hours.

Direct comparison of PET and MRI signal revealed that in vivo discordancy may occur at the high concentration range of ESIONs or when they are internalized into the intracellular space.

Micelle encapsulated ESIONs, with relatively long blood circulation time and rapid excretion through the hepatobiliary system, are promising T1 contrast agent which can potentially offer both efficiency and safety. Furthermore, radiolabeled ESIONs, by complementing each other's strengths and weaknesses, can be further applied to monitor the microscopic distribution in various clinical situations.

Student Number: 2016-30724

Table of Contents

List of Figures

6

List of Tables

List of Abbreviations

Abbreviations	Full name
PET	Positron emission tomography
MRI	Magnetic resonance imaging
TR	Repetition time
TE	Echo time
TAC	Time-activity curve
IONPs	Iron oxide nanoparticles
USPIO	Ultrasmall superparamagnetic iron oxide nanoparticles
ESIONs	Extremely small-sized iron oxide nanoparticles
RES	Reticuloendothelial system
Gd	Gadolinium
CT	Computed tomography
VOI	Volume of interest
MIP	Maximal intensity projection
SIR	Signal intensity ratio
%ID	Percent of injection dose
TEM	Transmission electron microscopy
d_H	Hydrodynamic diameter

ROS	Reactive oxygen species
PEG	Polyethylene glycol
TME	Tumor microenvironment
SAR	Specific absorption rate
PBS	Phosphate buffered saline
ITLC-SG	Instant thin layer chromatography-silica gel
^{64}Cu	Copper-64

Introduction

Nanomedicine is a term referring to an emerging field of medicine using nanomaterials. Nanomaterials are in a size range similar to the biological substances used by our own living organisms, yet can be intentionally designed, functionalized, produced, and applied (1). Regarding these points, nanomaterials have a potential advantage for medical applications.

Iron oxide nanoparticles (IONPs) are one of the few nanomaterials that can be applied clinically with FDA approval. As our body contains quite a lot of iron and stores it in ferritin, IONPs are well known to be a biocompatible nanomaterial. Various studies have been conducted for application in clinical fields such as tumor-targeted imaging (2), magnetic hyperthermia therapy (3, 4), drug delivery (5, 6), and live-cell tracking through cell labeling (7, 8). In particular, it has been applied in the clinical field for a long time as a magnetic resonance imaging (MRI) T2 contrast agent by utilizing superparamagnetic properties (9-11). The first generation IONPs, such as ferumoxide and ferucarbotran, have been mainly used for liver imaging agent (12-14). In normal liver after administration, most IONPs are taken up by the Kupffer cell, showing a low signal in T2 contrast MRI, whereas due to the absence of the Kupffer cell, IONPs are not taken up in the tumor tissue, resulting in a relatively high signal compared to the normal tissue. However, due to their large size (d_H ~50-200nm), IONPs were quickly cleared from the blood pool, and as a result, the clinical application was limited. Ultrasmall superparamagnetic IONPs (USPIO), with a hydrodynamic size of 20-50 nm, was introduced in 1990 as a next-generation imaging agent (9). They had an optimal size to avoid reticuloendothelial system (RES) uptake, resulting in a longer blood circulation,

which made them possible for versatile clinical applications, such as lymph node imaging (15-18), plaque imaging (19) and central nervous system macrophage imaging (20, 21). However, there is an inherent limitation in the case of T2 contrast agents producing negative signals (22, 23). Simply, the signal in the region of interest may be difficult to distinguish due to the influence of surrounding hypointense lesions and organs. Furthermore, the 'blooming effect' may occur due to high magnetic properties altering the local magnetic milieu, exaggerating the lesion, and blurring the image. Consequently, the clinical use of several iron oxide imaging agents has been discontinued in the United States and most of Europe (24).

On the contrary, the T1 contrast agent with a positive signal is relatively preferred in the clinical practice due to its high sensitivity. The T1 contrast effect is induced by shortening the longitudinal (T1) relaxation time of protons of a water molecule, which is the result of the interaction with an electron of contrast agents (25). Thus, paramagnetic compounds with more unpaired electrons may generally be more effective T1 contrast agents. Gadolinium (Gd) has 7 unpaired electrons and strong paramagnetic properties. Since the first Gd-based complex was approved by the FDA as an MRI contrast agent in 1988, more than 10 million MRI studies are currently conducted annually. Although Gd is the most widely used contrast agent in clinical practice, short-term and long-term safety issues have been continuously raised. The current consensus is that possible degradation of some Gd-based complexes, but not all, may induce nephrogenic systemic fibrosis in patients with renal impairment (26, 27). Furthermore, retention of Gd, although trace amount, has been recognized in a few organs, such as brain, skin, and bone (26, 28). To date, the clinical significance of such retention is not clearly known, but there is a concern that it may cause any long-term safety issue. To avoid these

degradation retention problems, Gd-complexes with stable and short blood circulation time has been developed, but their rapid clearance acts as a significant limitation when a relatively longer monitoring period is required (29). In view of these points, a next-generation T1 contrast agent with long blood circulation time and rapid body clearance is required for clinical application.

Interestingly, recent studies have shown IONPs' possibility as a T1 contrast agent (22, 30-33). The two main components to define the behavior of T1 contrast agents are longitudinal relaxivity (r_1) and relaxivity ratio (r_2/r_1). From the viewpoint of relaxation, a high r_1 value and a low r_2/r_1 ratio (close to '1') are characteristics of an ideal T1 contrast agent (25). Iron has 5 unpaired electrons, which is sufficient enough to interact with a proton in water molecules and reduce T1 relaxation time, indicating high r1 value. Indeed, USPIO has been used as a blood pool imaging agent (34-36). However, IONPs including USPIO commonly have high r_2 value and as a result, high r_2/r_1 ratio, due to its strong magnetic property, which limits its usage as an effective T1 contrast agent. Thus, reducing the magnetic property is the key strategy to make IONPs as T1 contrast agent. With decreasing nanoparticle size, magnetization decreases due to increased surface effects and reduced core volume. Accordingly, recent studies have recognized that extremely small-sized IONPs (ESIONs), smaller than 5 nm, can be a potential T1 contrast agent (37). Moreover, as IONPs have an advantage regarding biocompatibility, safety, and sufficient blood circulation time, they are expected to be a next-generation positive contrast agent.

Since most of the inorganic nanoparticles, including IONPs, are originall y dispersed in organic solvents after synthesis (38), they require surface mod

ification with various surfactants before being exposed to the aqueous enviro nment for in vivo administration. Micelle encapsulation method, for hydrophilization of nanomaterials, was recently introduced by our group to make a quick and straightforward one-step method for producing multifunctional nanoparticles under mild condition (39). The beauty of this method relies on the use of combined multiplex amphiphiles with different functional groups simultaneously, which enables the achievement of surface multifunctionality by bonding of small molecules as a specific ligand and accessible radiolabeling. Furthermore, the micelle encapsulation method has advantages in terms of mass production and cost effectiveness.

For further clinical application of this micelle encapsulated ESIONs as a T1 contrast agent, studies regarding toxicity, biodistribution, pharmacokinetics, and optimal fate are necessary. However, at this time point, these data are lacking, and it is challenging to conduct such a study due to inherent limitations of in vivo MRI quantification. Firstly, relaxation measurement is typically nonlinear in the range of high contrast agent concentration (40, 41). Commonly T1 effect is dominant at low concentration, however, at the high concentration range as the T2-shortening effect increases, it results in signal quenching. Each MRI sequence also shows the maximum signal intensity in a different range of concentrations. Moreover, after in vivo administration, more factors affect the quantification. The contrast agents usually are not uniformly distributed and when internalized into the cell, their relaxation properties significantly change (42-44). After cell internalization, MRI contrast agents normally are clustered inside the cellular components. Here, contrast agents cannot preferentially interact with protons of water molecules, and clustering increases local concentration and thus increases magnetization capacity.

As a result, the signal of the T1 contrast agent quenches after cell internalization. Lastly, protein binding and viscosity differences may alter the relaxivity.

Here radionanomedicine comes in (45, 46). In nuclear imaging, the observed effect is proportional to the injected concentration of radionuclide. Therefore, radiolabeling of the novel drug allow tracing the tracks and perform absolute quantification of injected radiolabeled compounds in the in vivo system, which can light upon the in vivo characteristics of biodistribution and optimal fate. Furthermore, only a trace amount of radionuclide is sufficient for pharmacokinetic study in vivo, which can offset concerns regarding the pharmacologic effect. Positron emission tomography (PET) imaging techniques used for radionanomedicine, provide many orders of magnitude higher sensitivity than that of computed tomography (CT) or MRI (47). PET imaging, of course, has a detection range. However, radioactivity can be controlled regardless of the amount of ligand, and if the amount of ligand is constant, it shows a uniform distribution Thus, when knowing the amount of injected radionuclide, you can evaluate the distribution intuitively and quantify accurately.

The recent development of PET/MRI system, with fine spatial resolution, high sensitivity, high temporal stability, and minimal mutual interference, made simultaneous imaging of multimodal imaging probes possible (48-50). The combination of the two modalities, complementing each other's strengths and weaknesses, appears to play an important role in the clinical field. Although many interesting multimodal imaging probes have been suggested, their spatiotemporal characteristics have been investigated using each imaging device separately. Sequential image acquisition makes the exact correlation and comparison studies of

multimodal imaging probes impossible (51, 52). Using simultaneous PET/MRI we can evaluate the in vivo fate of multimodal probe at the same time point and enables direct comparison, which is the actual beauty of multimodal imaging (53).

Purpose

In this study, I defined the in vitro characteristics of micelle encapsulated ESIONs and demonstrated the in vivo biodistribution and pharmacokinetics using radiolabeled ESIONs. A direct comparison of PET derived radioactivity and MRI signal intensity was demonstrated using simultaneous PET/MRI.

Materials and Methods

Synthesis of ESIONs

The ESIONs with 3 nm core size were synthesized based on the thermal decomposition method as described in a report by Park et al. (54) and were provided from Lee's group (Kookmin Univ.). Briefly, iron-oleate complex (oleic acid & oleyl alcohol) was dissolved in diphenyl ether at room temperature. The mixture was heated to 250°C at a constant heating rate of 10°C /min and then kept at this temperature for 30 min under an inert atmosphere. After the reaction, the mixture containing the nanoparticles was rapidly cooled to room temperature, and 50 mL of acetone was added to precipitate the nanoparticles. The nanoparticles were separated by centrifugation and dispersed in chloroform.

Radiolabeling of micelle encapsulated ESIONs

Three steps are required for the radiolabeling of hydrophilized ESIONs (Figure 1). All steps are based on encapsulation with micelles in one pot, and in the last step, isotopes are labeled with NOTA chelators doped on the micelle surface.

Micelle preparation, as the first step, was followed by the previous method (39), but the experiment was conducted with a slight modification for the large-scale encapsulation. Briefly, tween 60 solutions at concentrations of 10% (v/v) in distilled water (100 mL) were sonicated and heated for 30 min. Then, compared with the Tween60 mole number, 2 mol% of NOTA-SA was added and micelles

were re-formed with the same reaction temperature and time.

ESIONs was uniformly dispersed in the Tween60 micelle solution at the second step. After the removal of chloroform, 100 mg of ESIONs was added to 40 mL of micelles, and the remaining $CHCl_3$ was completely removed by stirring at room temperature. The mixture was sonicated for 30 min using bath type sonicator at 60°C. After sonication, the reaction mixture was centrifuged and purified at 40 000 rpm and 4°C for 2 h using OptiPrepTM gradients. After purification, the gradient was removed by an Amicon filter (Amicon Ultra-0.5, 100 kDa, Merck Millipore, 10000 rpm, 25°C, 2 min).

Radiolabeling was conducted at the final step. Radioisotope (^{64}Cu) containing vial was blown-dried by dry N_2 gas in the hood. After the vial was completely dried, 500 µL of 1 M sodium acetate buffer (pH 5.3) was added to reach pH 5. The 1 mL of encapsulated ESIONs was added and incubated at room temperature for 30 min. After radiolabeling, for the purification and neutralization, the buffer and unlabeled radioisotopes were removed by an Amicon filter (Amicon Ultra-0.5, 100 kDa, Merck Millipore, 10000 rpm, 25°C, 2 min). Radiolabeling efficiency was determined using radio-instant thin layer chromatography-silica gel (radio-ITLC-SG) after the radiolabeling procedure with citric acid (retardation factor (R_f) of free radioisotope = 0.9-1.0; R_f of radiolabeled ESIONs = 0.0-0.1) as the mobile phase.

Preparation of radiolabeled ESIONs
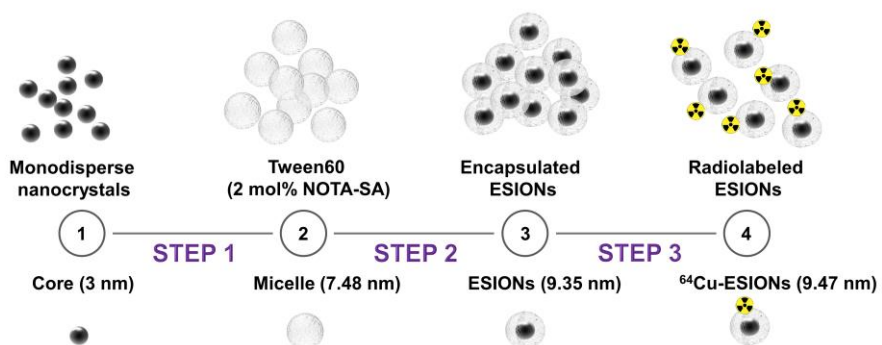
Figure 1. Schematics of stepwise radiolabeling process

Characterization of ESIONs

The hydrodynamic diameter and size distribution of micelle, micelle encapsulated ESIONs and radiolabeled ESIONs were analyzed by a dynamic light scattering (DLS) system Zetasizer Nano ZS90 (Malvern Instruments Ltd, Worcestershire, UK). Radiolabeled IONP (20 μL) was dissolved in distilled water (1 mL). The measured particle size and distribution were obtained in the mean number-percent (%) value. The average value was determined by measuring 5 times at 25°C at a scattering angle of 90°.

The T1 and T2 relaxation times of micelle encapsulated ESIONs and radiolabeled ESIONs were measured using a 1.41 T minispec mq 60 NMR Analyzer (Bruker, Germany) at 37°C. Relaxivity values were calculated via linear least-squares fitting of 1/relaxation time (s^{-1}) vs. the iron concentration (mM).

To determine the pH-dependent characteristic change of micelle encapsulated ESIONs, 0.5 ml of ESIONs (1 mgFe/ml) were added to 1.5 ml of buffer solutions with different pHs. The hydrodynamic diameter, size distribution, and relaxation properties were measured.

Stability Test

The stabilities of radiolabeled ESIONs were determined by ITLC-SG plates (Pall Corp., U.S.A.) with 0.1 M citric acid. The ITLC-SG strip was scanned using a TLC scanner (AR-2000, Bioscan, U.S.A.). The stability test of radiolabeled ESIONs on storage condition was examined in phosphate-buffered saline (PBS) at

room temperature for baseline, 1, 4, and 24 hours. Furthermore, the stability of radiolabeled ESIONs in human serum was also investigated. 0.1 mL of radiolabeled ESIONs were mixed with 1 mL of human serum, followed by incubation at 37°C. Before the test, human serum was filtered with Minsart syringe filter (0.2 µm, Sartotius stedim biotech, NY, USA). At baseline, 1, 4, and 24 hours, the radiochemical purity of the radiolabeled IONP solutions with human serum was tested as described above.

Animal study

All animal studies were conducted under approval by the Institutional Animal Care and Use Committee at Seoul National University. Specific pathogen-free 6-week-old male BALB/c mice were purchased from Orient Bio (Seongnam, Korea).

All PET/MRI data used in this study were acquired using SimPET (Aspect imaging, Shoham, Israel) simultaneous PET/MRI system. The SimPET system consists of 1-T permanent magnet-based MRI and novel SiPM-based PET insert, which has advantages not only in performance but also in installation space, maintenance, and stability (48). The SimPET insert has a peak sensitivity of 3.4% and center volumetric resolution of 0.53 mm^3 (49, 50).

The animal experiment consists of 3 parts (Figure 2).

Part 1. Biodistribution of Micelle encapsulated-ESIONs

Image-based in vivo biodistribution of radiolabeled ESIONs was evaluated using simultaneous PET/MRI in BALB/c mice (n = 3). ^{64}Cu-IONP with an iron concentration of 5 mgFe/kg (dose = 11.25 ± 0.7 Mbq/200 ul) was injected into the mice through the tail vein. Before the injection, the pre-MRI scan was obtained using a 3-dimensional (3D) T1-weighted gradient echo (GRE) sequence (TR/TE, 9/2.8 ms; Flip angle, 45 degrees). Dynamic PET imaging was acquired for 56 minutes right after the injection of radiolabeled ESIONs and later reconstructed to 8 sequential images with 7 min interval. Simultaneously, 3D T1-weighted GRE MRI images were acquired with the same 7 min interval. PET/MRI images of serial time points were further acquired at 2, 3, 4, 24, 48, and 72 hours after injection for 7 min. Acquired images were reconstructed using a 2D ordered-subsets expectation maximization algorithm with scatter and decay correction. The volume of interest (VOI) was manually drawn over the major organs (heart, liver, spleen, kidney, and lung) and excretory organs (intestine and bladder) on MRI images of mice acquired at different time points. The radioactivity in the organs from different sized radiolabeled ESIONs was estimated by applying the VOI (drawn on MRI images) over the organs on respective PET images acquired simultaneously. The activity (Bq) measured in the organ was normalized to the total injected dose of each radiotracer and divided by the volume of respective organs to obtain percentage injected dose per volume (%ID/ml). The PET image-based biodistribution was plotted as a function of time to generate time-activity curves (TACs). Feces and urine were collected, to evaluate the in vivo stability and excretion of the ^{64}Cu-ESIONs, at 1 and 4 hours after injection. The stability of radiolabeled ESIONs in excreted materials was determined by ITLC-SG and the iron concentration was measured for each excreta.

Ex vivo biodistribution of radiolabeled ESIONs was further evaluated. After injection of ^{64}Cu-IONP (dose = 1 µCi/100 µL), mice were sacrificed at serial time points of 5 min, 1, 4, and 24 hours (n = 3, respectively, total = 12). Urine and feces were collected from 0 to 4 hours and from 4 to 24 hours. Radioactivity of blood, major organs (heart, lung, liver, spleen, stomach, intestine, and kidney) and excreta (urine and feces) was counted using a gamma scintillation counter (DREAM r-10, Shinjin Medics Inc., South Korea). The stability of radiolabeled ESIONs in blood samples acquired at different time points (5min, 1, and 4 hours) was evaluated using ITLG-SG.

Part 2. Direct Comparison of PET and MRI signal in vivo

Blood Pool

Data regarding image-based in vivo biodistribution from Part 1. was used to compare the blood pool signal between the PET and MRI. For the quantitative evaluation of vascular contrast enhancement in the MRI, signal intensity ratio (SIR) was calculated in the VOI of heart as following.

$$SIR = \frac{post-contrast\ signal\ intensity}{pre-contrast\ signal\ intensity}$$

SIR of MRI and %ID/ml acquired from PET at the same time point was compared.

A phantom study was conducted to further define the dose-dependent signal difference of each modality. A radiolabeled ESIONs were diluted into 5 different concentrations. At each step, ESIONs were diluted to half of the previous

concentration starting from 1 mM (dose = 2.6 MBq/ml). The diluted ^{64}Cu-ESIONs and normal saline, as a control, were filled into plastic vials and embedded into a plastic container that has multiple crafted holes for vial insertion. The container was placed in a perpendicular direction to the main magnetic field and the same PET/MRI protocol, as done in the biodistribution study, was applied. Circular VOI was drawn over each vial inserted holes for the quantification.

Dose-dependent change of blood pool MRI signal was evaluated in vivo using ESIONs with 3 different concentrations (2.5 mgFe/kg, 5 mgFe/kg and 10 mgFe/kg). Ten sequential images of 3D T1-weighted GRE with 3.5 min interval was acquired right after the injection of ESIONs with different concentration. An additional 1.5-hour MRI image was acquired. For the quantitative evaluation of vascular contrast enhancement, SIR was quantified using the manually drawn VOI of the aorta.

Liver

Quantitative values derived from Part 1. was used to compare the liver signal between the PET (%ID/ml) and MRI (SIR) obtained simultaneously.

To reflect the internalized fraction, retention fraction of radiolabeled ESIONs was obtained at each time point. The washout liver model was used to compare the cell retention fraction and MRI liver signal (SIR). After injection of ^{64}Cu-ESIONs, with iron concentration of 5 mgFe/kg (dose = 13.23 ± 0.42 Mbq/200 ul), mice were sacrificed at serial time points of 5 min, 1, 4 and 24 hours (n = 2, respectively, total = 8). The liver was extracted after ligation of the portal vein, hepatic artery, and the inferior vena cava. Radioactivity (pre-radioactivity) of the liver was counted using a gamma

scintillation counter. Afterward, radiolabeled ESIONs in the blood pool were removed by perfusion through the portal vein using warm normal saline. Post-radioactivity was counted and cell retention fraction of radiolabeled ESIONs in the liver was calculated as follows.

$$Retention\ fraction = \frac{post-radioactivity\ count}{pre-radioactivity\ count}$$

Part 3. Monitoring microscopic distribution of radiolabeled ESIONs in vivo

As a proof of concept study, the microscopic distribution of ESIONs was evaluated in the tumor model, 4 hours after intratumoral injection of ^{64}Cu-IONP (dose = 2.68 ± 0.13 Mbq/50 ul). Tumor xenograft models were provided by Seok's group (Seoul National Univ.). Briefly, 2x105 4T1-Luc2 cells were injected into the inguinal right fourth mammary fat pad of 7 week-old female BALB/c mice and were used in the study, 21 days after injection.
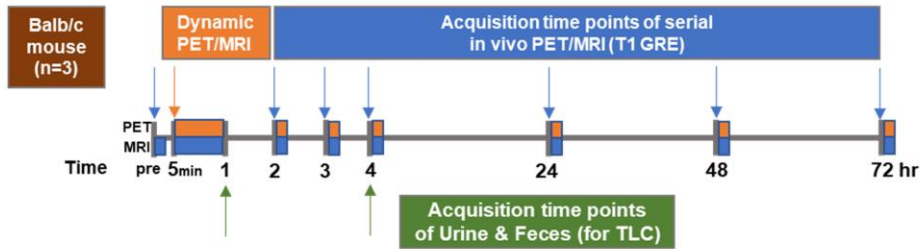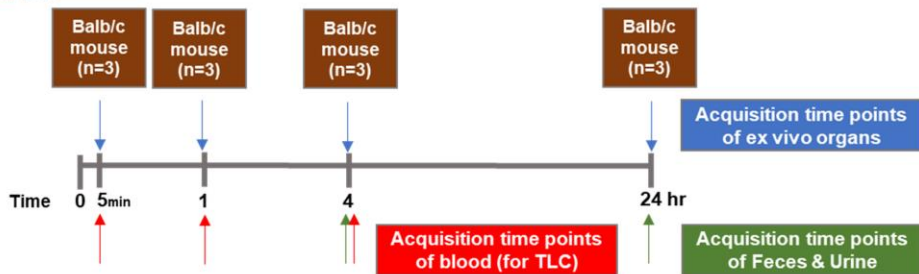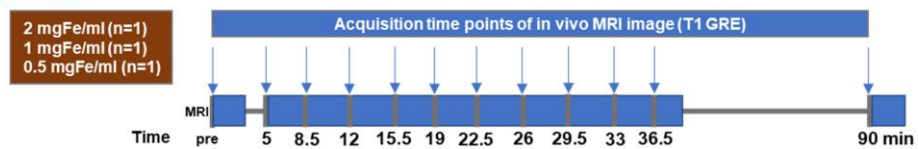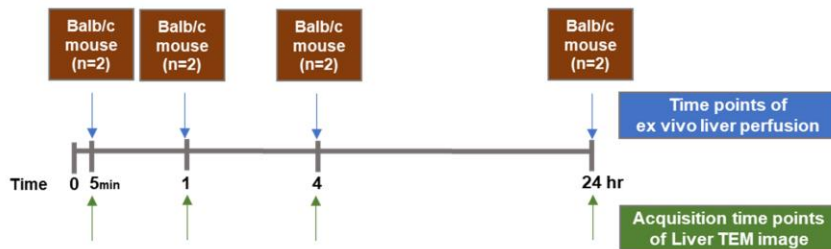
Figure 2. Experimental design

27

In vivo experimental design consists of 3 parts. **Part 1.** Biodistribution of ^{64}Cu-ESIONs; **Part 2.** Direct comparison of PET and MRI signal in vivo; **Part 3.** Monitoring microscopic distribution of radiolabeled ESIONs in vivo

Transmission electron microscopy (TEM)

Transmission electron microscopy (TEM) images of liver tissue at each time point and tumor tissue were acquired to further investigate the microscopic distribution of ESIONs. TEM images were taken at an acceleration voltage of 80 keV (JEM-1400; Jeol). Liver tissue of 5 min, 1 hour, 4 hours and 24 hours after ESIONs injected mice was chopped and multiple pieces were selected including different 4 regions of both lobes of the liver.

Concentration measurement

Inductively coupled plasma mass spectrometer (ICP-MS, ELAN 6100, Perkin-Elmer, Massachusetts, USA) at National Center for Inter-university Research Facilities (NCIRF, Seoul National University) was used to estimate the concentration of core IONPs.

The concentration of micelle encapsulated ESIONs and radiolabeled ESIONs was measured using NanoDrop 2000c Spectrophotometer (Thermo Scientific, USA). Briefly, ESIONs were all decomposed to iron ion in nitric acid solution and incubated at room temperature for 30 min. Then KSCN solution was added, and as the color of the solution change to red, the wavelength of the mixture was detected by the Spectrophotometer. The concentration was calculated by incorporating the measured absorbance into the standard curve extracted from the standard $Fe(NO_3)_3$ solution.

Results

pH-dependent characteristic change of ESIONs

Micelle, as an anionic surfactant, commonly induce negative charge to the nanoparticle after encapsulation. This negative charge leads to electrostatic repulsion between the encapsulated nanoparticle and stabilizes it. However, when introduced to the acidic pH, through protonation, the surface charge of the nanoparticle may become near neutral, which can cause aggregation of particles (55, 56). In this study, the labeling process is performed at acidic pH (pH 5.6) for effective labeling. Therefore, pH-dependent change of hydrodynamic size and MRI relaxation properties when exposed to acidic pH was observed.

After exposure to acidic pH, after a certain period, it was visually cloudy, and aggregated particles could be observed in the TEM image (Figure 3a). The hydrodynamic diameters of micelle encapsulated ESIONs in neutral pH (baseline), pH6, and pH5 were 9.35 ± 2.20 nm, 736.12 ± 254.20 nm, and 116.32 ± 57.31 nm, respectively. When exposed to acidic pH micelle encapsulated ESIONs showed the bigger size and more scattered distribution compared with the baseline (Figure 3b).

In the same vein, relaxivity, especially T2 relaxation time, was highly variable at acidic pH. Due to the aggregation effect, r_2 was estimated to be high and as a result r_2/r_1 was high compared to the micelle encapsulated ESIONs (Figure 4). The detailed values are summarized in Table 1.

Comprehensively, since the acidic pH can affect the characteristics of micelle encapsulated ESIONs, in this study, the neutralization process through buffer exchange after radiolabeling was additionally performed.

30
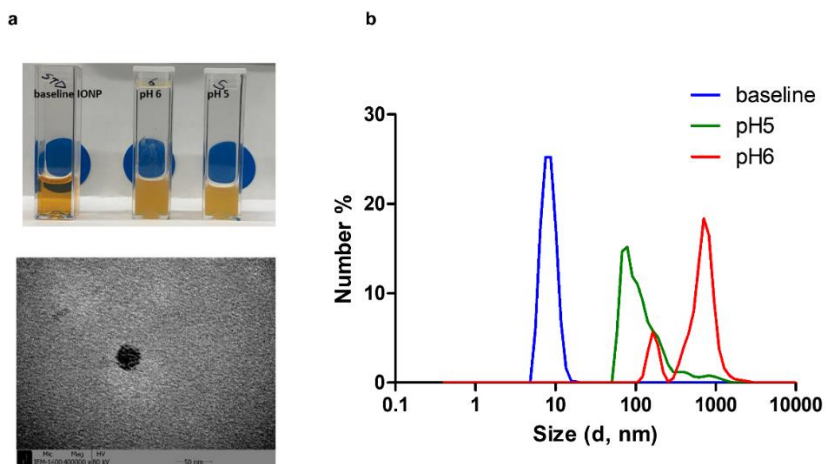
Figure 3. Hydrodynamic size of micelle encapsulated ESIONs in different pH

a, Micelle encapsulated ESIONs after exposure to an acidic pH was visually cloudy, aggregated in the TEM image, **b,** and showed a significant increase in hydrodynamic size.
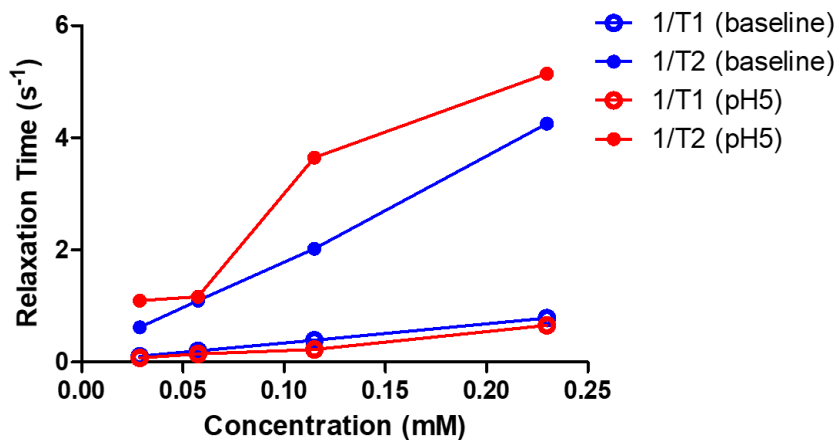
Figure 4. Relaxivity of micelle encapsulated ESIONs in different pH

Micelle encapsulated ESIONs after exposure to an acidic pH showed a lower r_1 value of 2.68 $s^{-1}mM^{-1}$ and a higher r_2/r_1 ratio of 9.03 compared to the baseline, which showed r_1 and r_2/r_1 ratio of 3.43 $s^{-1}mM^{-1}$ and 5.36, respectively.

Characteristics of radiolabeled ESIONs

The ESIONs core showed excellent uniformity on TEM, and there was no change in the micelle encapsulation process (Figure 5a).

The hydrodynamic diameters of the micelle, micelle encapsulated ESIONs, and ^{64}Cu-ESIONs were 7.48 ± 1.51 nm, 9.35 ± 1.28 nm, and 9.47 ± 2.20 nm, respectively. No significant change in size was observed after the radiolabeling procedure (Figure 5b).

Compared to baseline, relatively low r_1 value was observed in radiolabeled ESIONs, but similar r_2/r_1 ratio was observed (Figure 6). Thus, radiolabeling process of micelle encapsulated ESIONs did not significantly alter the relaxivity. Furthermore, micelle encapsulated ESIONs and radiolabeled ESIONs are expected to have sufficient performance as a T1 contrast agent, with relatively low r_2/r_1 ratio. The detailed values are summarized in Table 1.
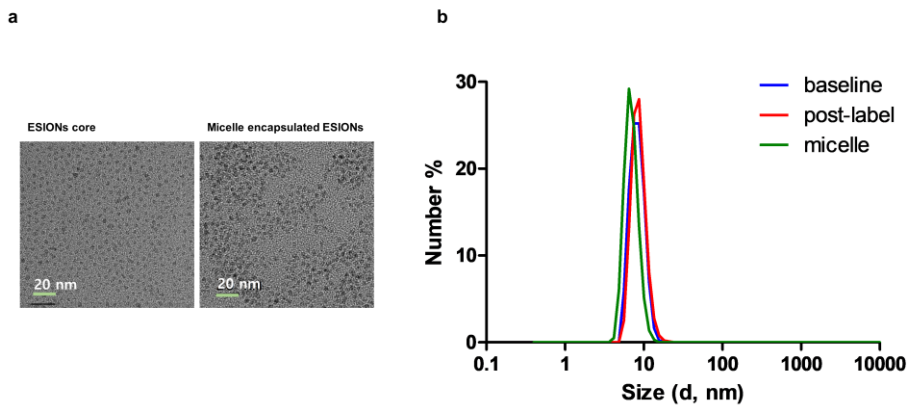
Figure 5. Size of the micelle, micelle encapsulated ESIONs, and radiolabeled ESIONs

a, The shape and visual size of the ESIONs core were not changed on TEM image after micelle encapsulation. **b,** The hydrodynamic diameters of the micelle, micelle encapsulated ESIONs (baseline) and ^{64}Cu-ESIONs (post-label) were 7.48 ± 1.51 nm, 9.35 ± 1.28 nm, and 9.47 ± 2.20 nm, respectively.
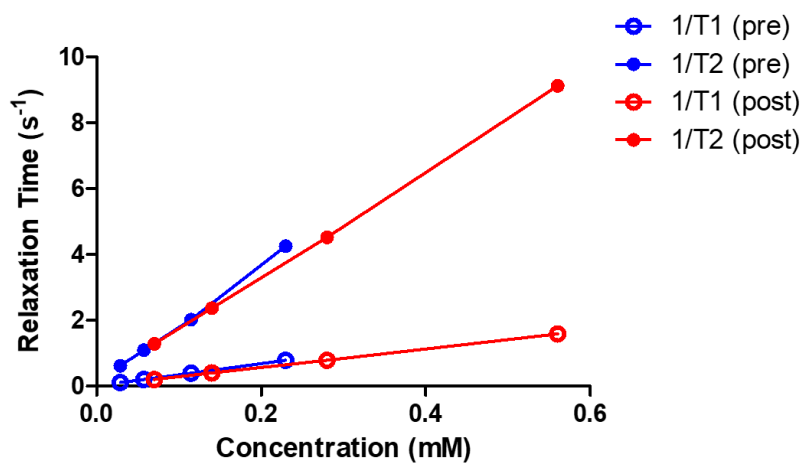
Figure 6. Relaxivity of micelle encapsulated ESIONs and radiolabeled ESIONs

After radiolabeling, r_1 value (2.83 $s^{-1}mM^{-1}$) was estimated to be low compared to that of baseline (3.43 $s^{-1}mM^{-1}$). However, no significant change in the r_2/r_1 ratio was observed after radiolabeling (baseline vs post-label, 5.76 vs 5.36).

Characteristics		pH5	Baseline	Post-label
Relaxivity	r_1 (s^{-1}mM^{-1})	2.68	3.43	2.83
	r_2 (s^{-1}mM^{-1})	24.24	18.40	16.31
	r_2/r_1	9.03	5.36	5.76
Hydrodynamic Size (mean ± SD, nm)		116.32 ± 57.31	9.35 ± 1.28	9.47 ± 2.20

Table 1. Characteristics of micelle encapsulated ESIONs in different conditions

Stability Test

Labeling efficiency of ^{64}Cu-ESIONs was over 95% and remained stable until 24 hours in PBS solution at room temperature (92.4%) and in human serum at 37 °C (77.1%) (Figure 7).
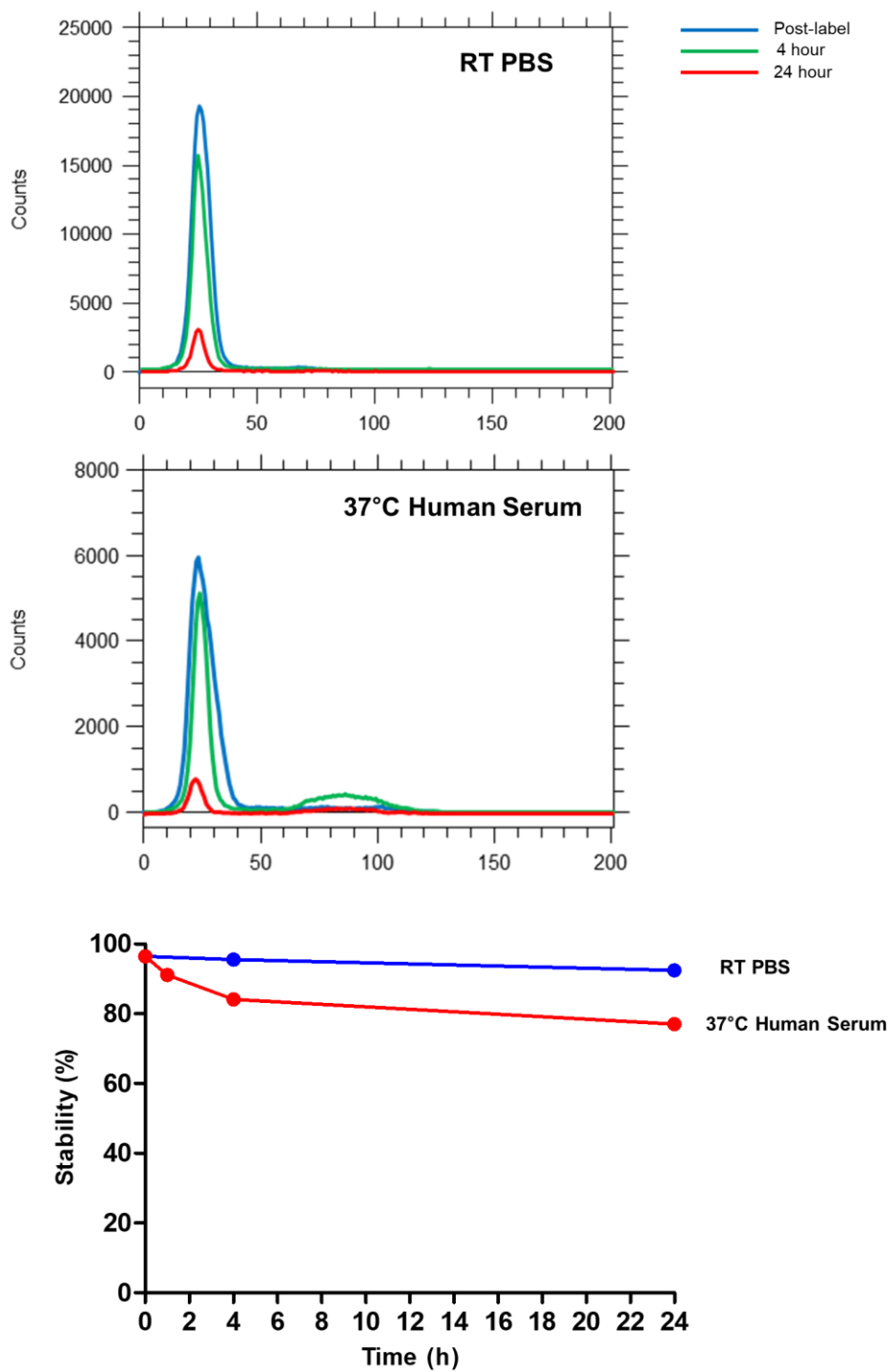
Figure 7. In vitro stability test

Part 1. Biodistribution of ^{64}Cu-ESIONs

Image-based in vivo biodistribution study

Serial PET images were obtained after ^{64}Cu-ESIONs injection and maximum intensity projection (MIP) images were demonstrated (Figure 8).

For the quantification, the correction factor was first obtained using a ^{64}Cu phantom. Next, the %ID/ml value, of each organ at each time point, was measured from manually drawn VOI and it was expressed as TAC (Figure 9).

In the early time points, the radiolabeled ESIONs were mainly distributed among organs representing the blood pool, such as heart, great vessel, lung, and kidneys. A biphasic decrease of radioactivity in the blood pool was observed. In the early time point, the half-life was approximately 62 min and in the slowly decreasing phase, the half-life was measured to be approximately 12.8 hours. Minimal bladder uptake, suggesting a urinary excretion, was observed in the early hours. Over time, blood pool activity decreased, and the uptake of the liver and intestine increased up to 4 hours. Afterward, both the liver and intestine showed a gradual decrease in radioactivity, until 72 hours.
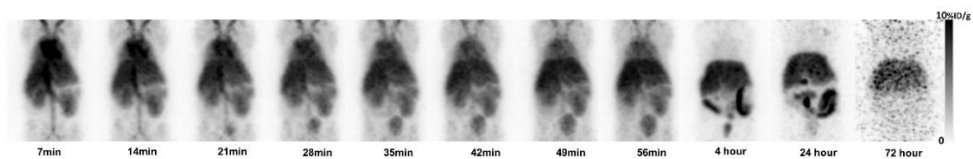
Figure 8. In vivo PET results of ^{64}Cu-ESIONs

Decay-corrected MIP (Maximum Intensity Projection) images in BALB/c mice at different time points after intravenous injection of ^{64}Cu-ESIONs were shown.
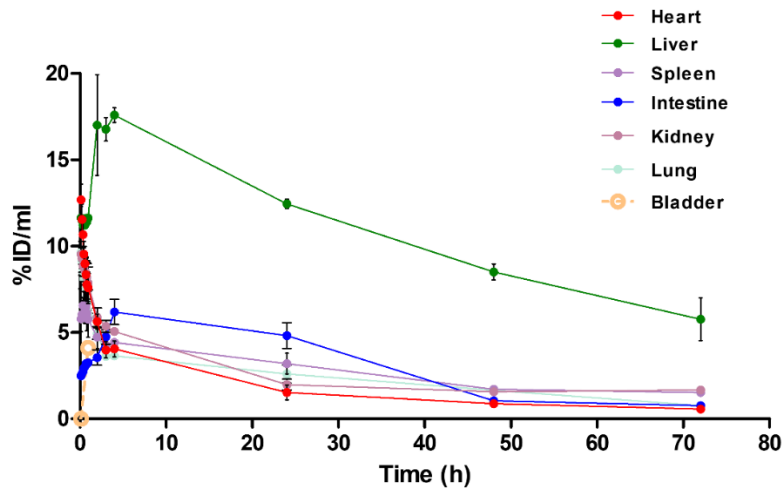
Figure 9. Image-based quantification of ^{64}Cu-ESIONs biodistribution

In vivo PET image of BALB/c mice after intravenous injection ^{64}Cu-ESIONs was quantitatively analyzed. Major organ uptake at serial time points was obtained and was expressed as mean $\pm$ SD (%ID/ml).

Ex vivo biodistribution study

The ex vivo biodistribution of ^{64}Cu-IONP was obtained in units of %ID/organ at each time point (Figure 10). The mean and standard deviation of %ID/organ are summarized in Table 2. Blood activity as an organ was first measured in %ID/g and then multiplied by 7% of the mouse weight, considering the mouse blood volume. Rapid clearance was observed in the blood, lung, and kidney. Still, a considerable amount of radioactivity remained in the blood at 1 hour and 4 hours, mean %ID/organ ± SD was estimated to be 15.98 ± 2.28 and 7.19 ± 1.03, respectively. Liver uptake peaked at 1 hour and gradually decreased until 24 hours. Intestinal uptake gradually increased until 4 hours and remained plateau. Urine and feces from injection to 4 hours and 4 to 24 hours were collected. The sum of urine and feces accumulated up to 24 hours was 4.45 ± 2.32 and 38.77 ± 3.11 respectively. Comprehensively, up to 40% of radiolabeled ESIONs were excreted through the hepatobiliary pathway within 24 hours.
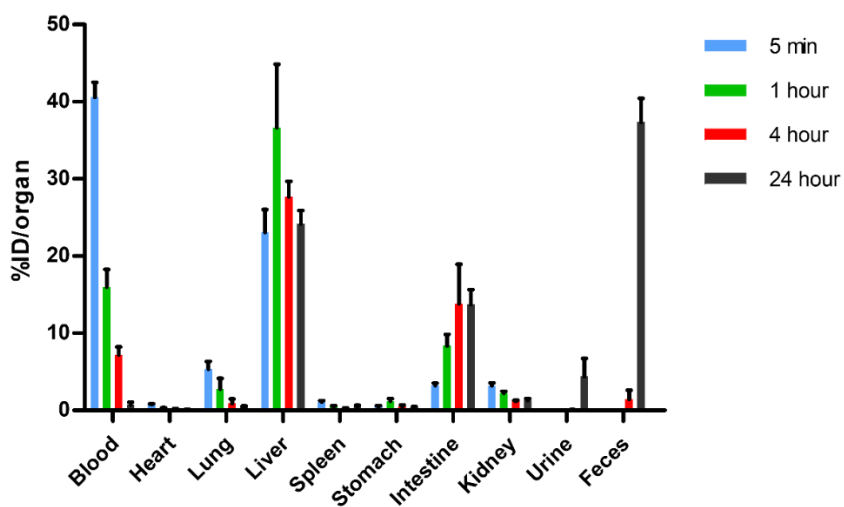
Figure 10. Ex vivo quantification of ^{64}Cu-ESIONs biodistribution

Ex vivo biodistribution of BALB/c mice after intravenous injection ^{64}Cu-ESIONs was quantitatively analyzed. Major organ uptake at serial time points was obtained and was expressed in units of %ID/organ.

Time		5 min	1 hour	4 hours	24 hours
Organs	Blood	40.55 ± 1.98	15.98 ± 2.28	7.19 ± 1.03	0.74 ± 0.33
	Heart	0.75 ± 0.08	0.34 ± 0.03	0.21 ± 0.02	0.09 ± 0.06
	Lung	5.35 ± 1.01	2.79 ± 1.37	0.90 ± 0.58	0.47 ± 0.10
	Liver	23.06 ± 2.96	36.63 ± 8.22	27.68 ± 1.99	24.18 ± 1.71
	Spleen	1.06 ± 0.22	0.44 ± 0.17	0.27 ± 0.06	0.50 ± 0.16
	Stomach	0.44 ± 0.14	1.21 ± 0.33	0.44 ± 0.23	0.36 ± 0.11
	Intestine	3.21 ± 0.33	8.36 ± 1.49	13.81 ± 5.14	13.73 ± 1.92
	Kidney	3.18 ± 0.38	2.22 ± 0.26	1.16 ± 0.17	1.28 ± 0.25
	Total	77.61 ± 4.58	67.97 ± 13.12	51.66 ± 4.10	41.37 ± 2.93
Excreta	Feces			1.43 ± 1.18	37.34 ± 3.11
	Urine			0.07 ± 0.02	4.38 ± 2.33

Table 2. Ex vivo biodistribution of ^{64}Cu-ESIONs in the major organs (%ID/organ)

In vivo stability

From the pharmacokinetic study, excretion of radiolabeled ESIONs was mostly through hepatobiliary excretion and some portion as urine. To confirm the composition of excreta and evaluate the in vivo stability, the radiochemical purity of urine, blood, and feces was estimated using ITLC-SG.

ITLC-SG result of the urine collected one hour after an injection of ^{64}Cu-ESIONs revealed that most of the radioactivity was detected as a disintegrated form (Figure 11a). Furthermore, spectrophotometry revealed no measurable concentration of iron in the urine (Figure 11b).

Almost identical peaks with that of ^{64}Cu-ESIONs were observed from the blood, collected at 5 min, 1 hour, and 4 hours.

Stool contents were collected from the large bowel at 4 hours after injection of ^{64}Cu-ESIONs and mixed with normal saline. The mixture of stool samples showed contrast enhancement in 3D T1-weighted GRE MRI and at the same time radioactivity in PET image. As a result of supporting this, ITLC-SG revealed high radiochemical purity (81%) of ^{64}Cu-ESIONs in the stool sample (Figure 13).
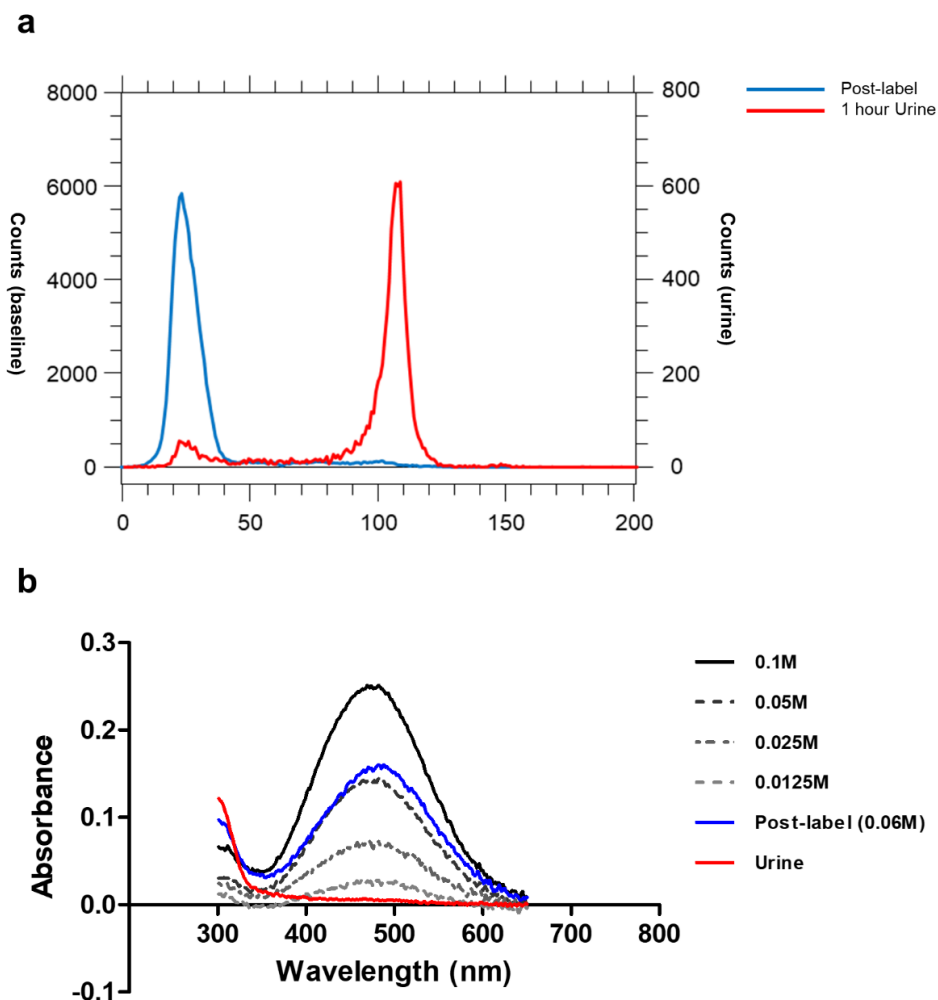
Figure 11. Radiochemical purity test of urine sample

A urine sample was collected, 1 hour after administration of ^{64}Cu-ESIONs. **a,** Radioactivity of urine was mostly detected as a disintegrated form. **b,** As a result of measurement using spectrophotometry, iron was not detected in the urine sample.
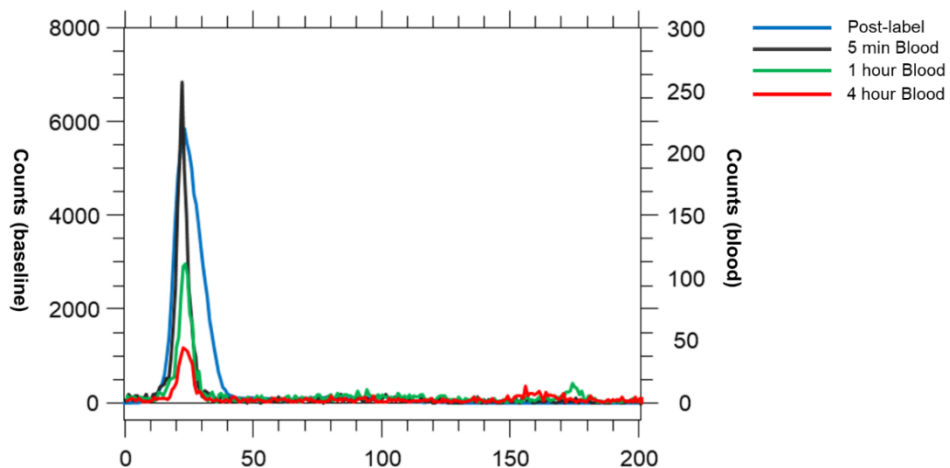
Figure 12. Radiochemical purity test of blood sample

A blood sample was collected at different time points (5 min, 1 hour, and 4 hours) after administration of ^{64}Cu-ESIONs. Radioactivity of blood was mostly detected as an intact form.
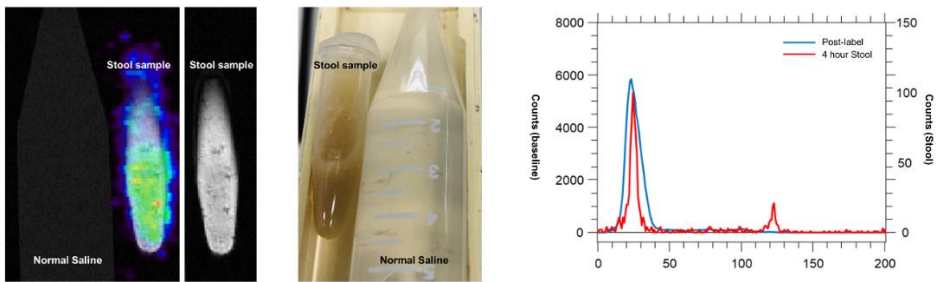
Figure 13. Radiochemical purity test of stool sample

A stool sample was collected, 4 hours after administration of ^{64}Cu-ESIONs. The mixture of stool samples showed contrast enhancement in T1-weighted MRI with corresponding radioactivity. Radioactivity of blood was mostly detected as an intact form with radiochemical purity of 81%.

Part 2. Direct comparison of PET and MRI signal in vivo

Image-based comparison of blood pool signal

After injection of ^{64}Cu-ESIONs with an iron concentration of 5 mgFe/kg (dose = 11.25 ± 0.7 Mbq/200 ul), SIR from the 3D T1-weighted GRE MRI and %ID/ml acquired from the PET was compared.

In the early time point, SIR showed almost plateau value, but radioactivity rapidly declined. From 1 hour, both SIR and radioactivity gradually decreased with time and reach the plateau after 24 hours. The correlation graph showed that both signals were linear in the range with low radioactivity but relatively non-linear in the range with high radioactivity.
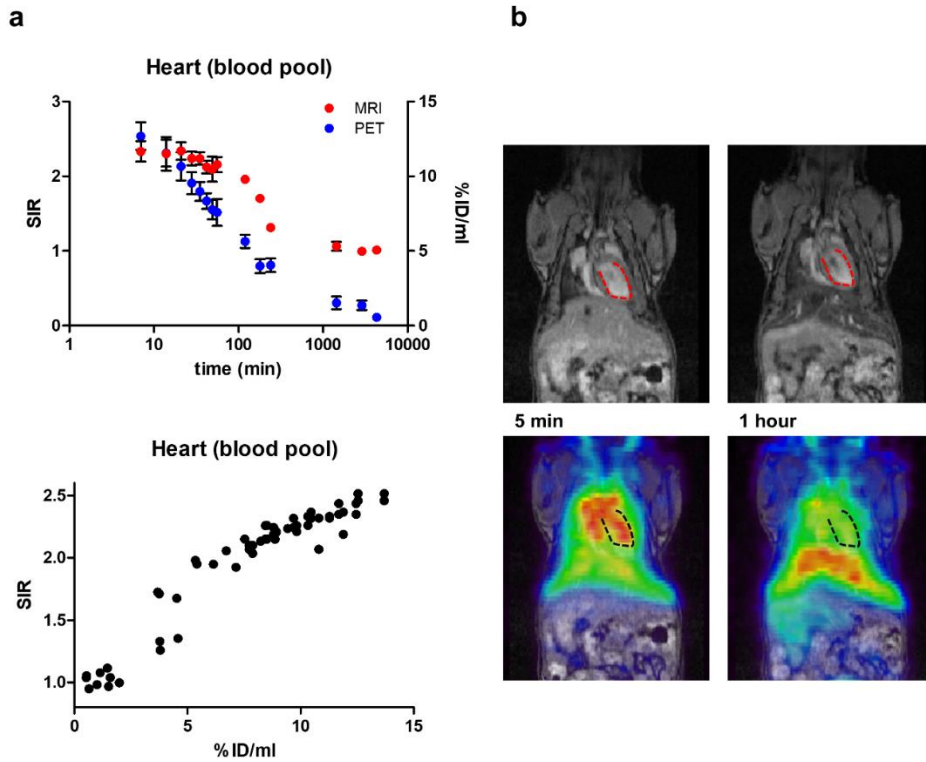
Figure 14. Direct comparison of PET and MRI blood pool signal in vivo

Time-dependent change of PET and MRI blood pool signal was compared after injection of ^{64}Cu-ESIONs with an iron concentration of 5 mgFe/kg. **a,** Time activity curve and correlation graph were obtained, as SIR representing MRI signal intensity and %ID/ml as PET radioactivity. **b,** Representative image showing persistent blood pool enhancement in the MRI, while a significant decrease of radioactivity was observed in the corresponding region.

Phantom study of dose-dependent signal change

A similar result was observed in the phantom study. PET and MRI signals, of ^{64}Cu-ESIONs solutions which were diluted sequentially in half, were measured. While the PET signal showed a linear distribution over the entire concentration range, the SIR value showed a relatively linear change with the concentration at a low concentration, but at a high concentration range, the signal rather decreased as the concentration increased (Figure 15).
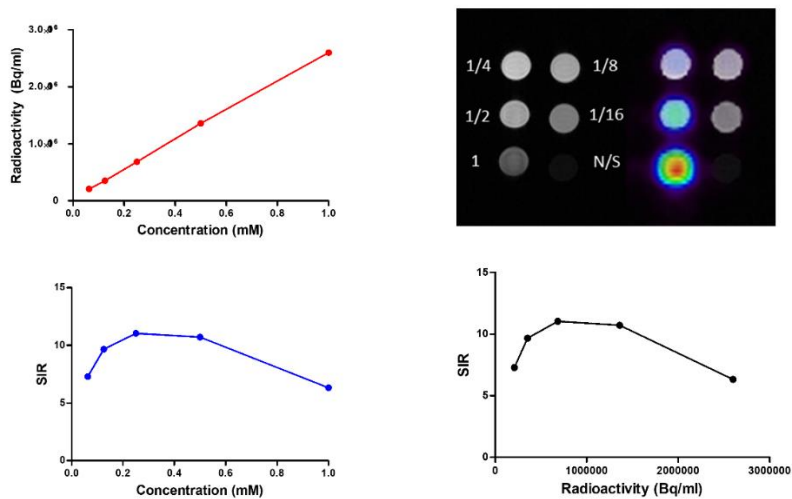
Figure 15. Direct comparison of PET and MRI signal in phantom

Concentration-dependent change of PET and MRI signal was compared using sequentially diluted ^{64}Cu-ESIONs. MRI signal intensity was expressed as SIR and PET as Bq/ml

Dose-dependent difference in MRI signal in vivo

Time-dependent change of blood pool MRI signal was further evaluated using 3 different concentrations of ESIONs (Figure 16). Linear decrease of blood pool signal over time was observed at a concentration of 2.5 mgFe/kg. Similar to the previous results, when 5 mgFe/kg was administered, a plateau of SIR value was shown initially and then the signal decreased at 1.5 hours. At the highest concentration of ESIONs, 10 mgFe/kg, SIR value was estimated to be the lowest in the early time point and the signal rather increased after 1.5 hours.
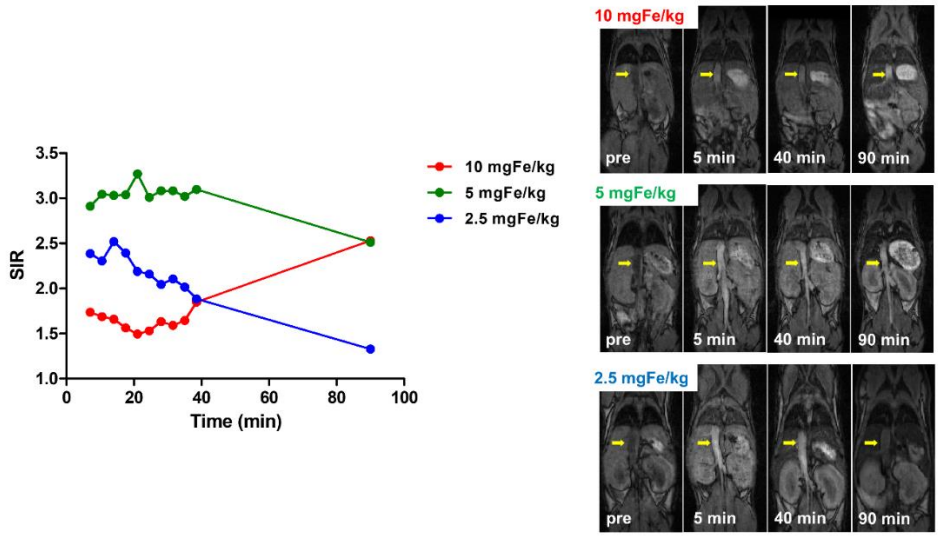
Figure 16. Comparison of time-dependent MRI signal change in different concentration in vivo

Time activity curve of SIR was compared between 3 different concentration (10 mgFe/kg, 5 mgFe/kg and 2.5mgFe/kg) of ESIONs.

Image-based comparison of liver signal

SIR value and %ID/ml of liver from serial PET/MRI were obtained after injection of ^{64}Cu-ESIONs with an iron concentration of 5 mgFe/kg (dose = 11.25 ± 0.7 Mbq/200 ul) and both values were compared. While the MRI signal gradually decreased over time, persistent uptake of ^{64}Cu-ESIONs was observed in the liver by PET (Figure 17).
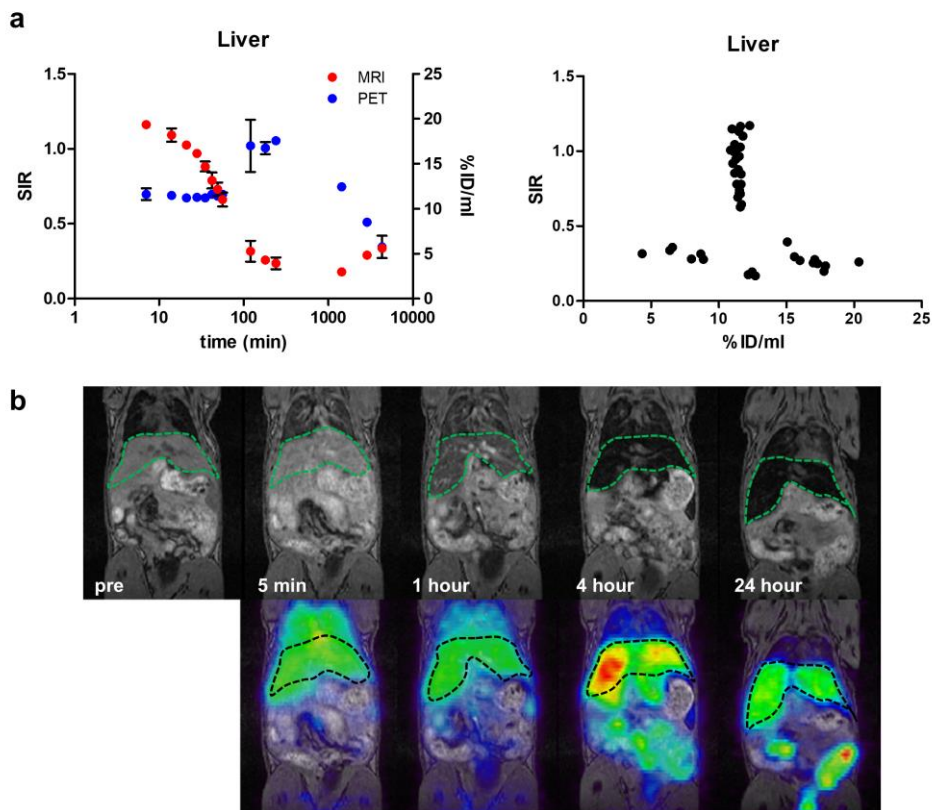
Figure 17. Direct comparison of PET and MRI liver signal in vivo

Time-dependent change of PET and MRI liver signal was compared after injection of ^{64}Cu-ESIONs with an iron concentration of 5 mgFe/kg. **a,** Time activity curve and correlation graph were obtained, as SIR representing MRI signal intensity and %ID/ml as PET radioactivity. **b,** Representative image showing a gradual decrease of MRI signal in the liver, while radioactivity is relatively maintained in the corresponding region.

Comparison between cell retention fraction and liver SIR

Retention fraction of radiolabeled ESIONs was obtained at each time point, using a washout liver model. Brief scheme and representative images of before and after washout are shown in Figure 18a. Retention fraction, starting from 64.1 % at 5 min, increased with time and reach the plateau at 4 hours. Compared with the liver SIR value, from the corresponding time point, retention fraction showed a negative correlation and linearity (Figure 18b).

a

IVC

Liver

Portal Vein

Normal Saline Perfusion

Pre
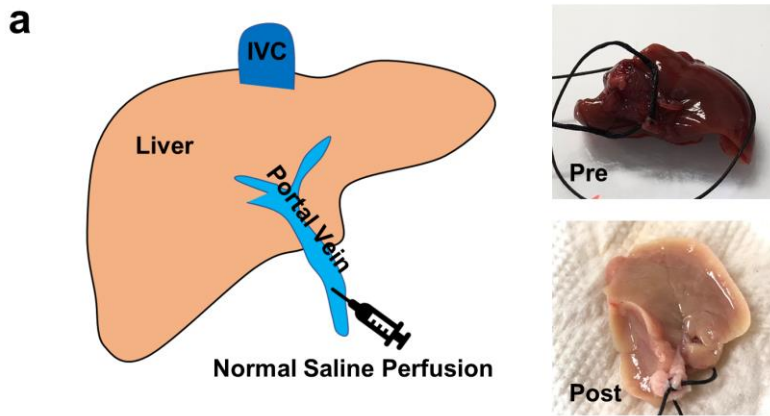
Post

$$Retention\ fraction\ (\%) = \frac{_{post}count}{_{pre}count} \times 100$$

b
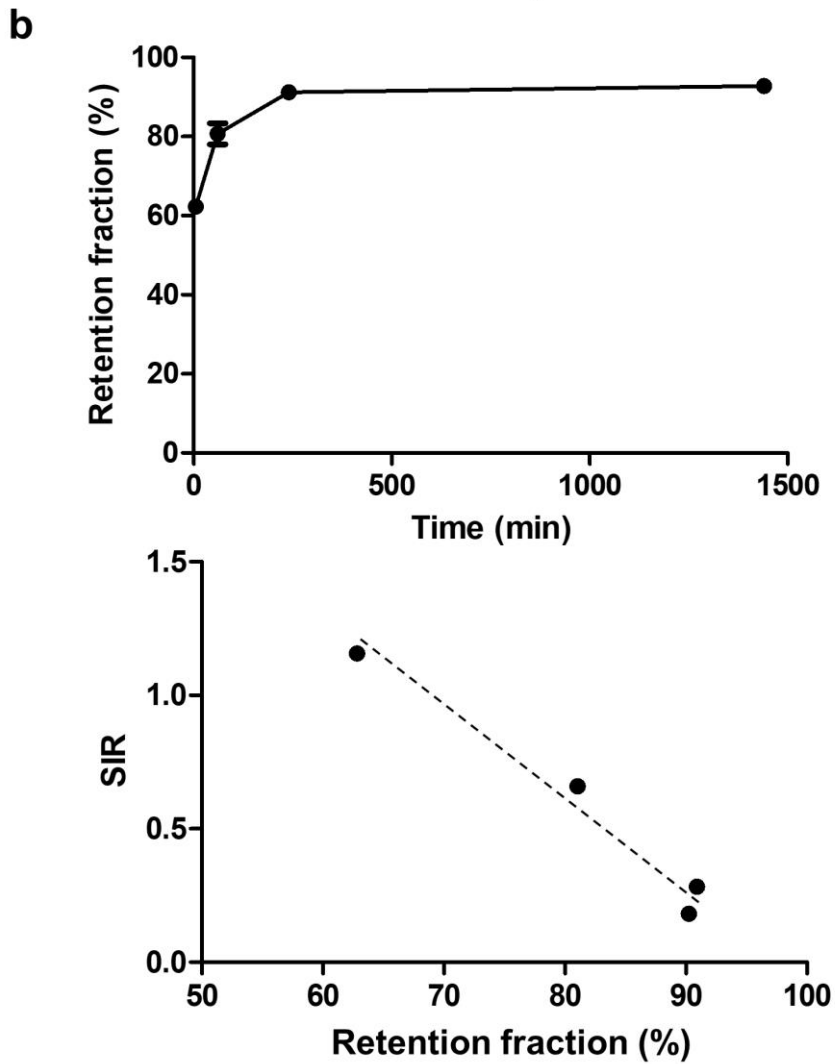
Figure 18. Comparison between cell retention fraction and liver SIR

a, Brief scheme and representative images of before and after washout. **b,** The retention fraction (%) of radiolabeled ESIONs was obtained at each time point, using a washout liver model, and was compared with SIR, representing an MRI signal.

TEM study of cell internalization in liver

The hepatic uptake and microscopic distribution of radiolabeled ESIONs were investigated using serial time point TEM image (Figure 19). At 5 min, ESIONs were observed in both the blood pool and intracellular compartments of endothelial cells and hepatocyte. While the ESIONs in the blood pool were freely distributed, intracellular ESIONs were clustered inside the cytoplasmic vesicles. ESIONs were more dominant in the intracellular components than the blood pool at 1 hour after injection. Compared with the earlier time point, ESIONs inside the endothelial cells were clustered in numerous lysosomes. Pinocytosis at the endothelial cell was observed from 5 min TEM image until 1 hour. At 4 hours, clustered ESIONs were observed in the lysosomes of the Kupffer cell. In the hepatocytes, vesicles containing IONP were frequently seen at the cell margin. ESIONs were rarely observed in the blood pool. Clustered ESIONs were still visualized, at 24 hours, inside the Kupffer cell, and some in the vesicles of the hepatocyte.

5 min
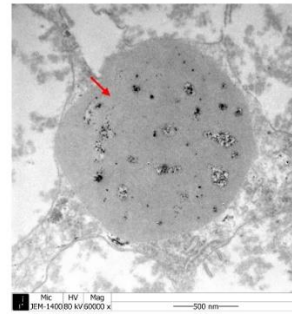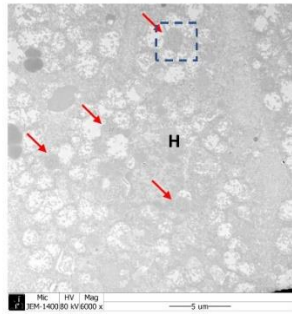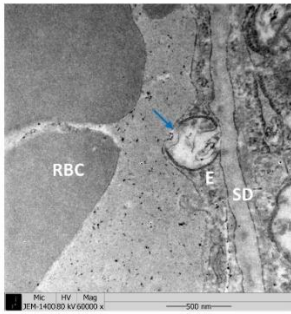
1 hour
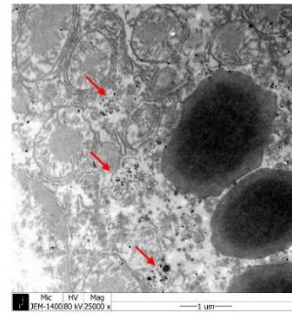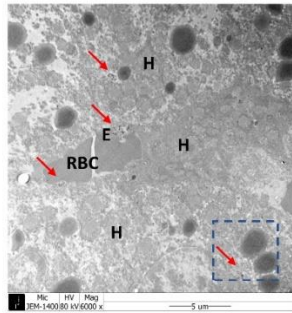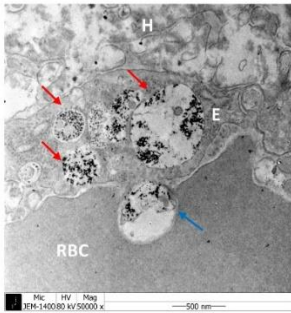
4 hours
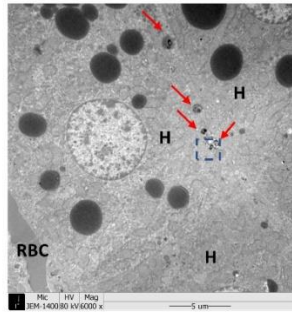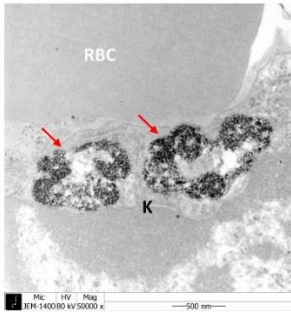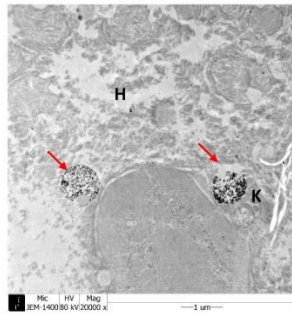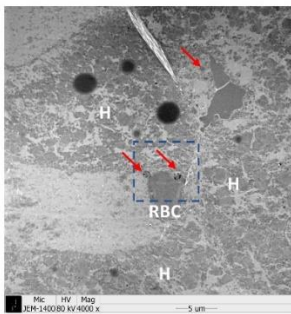
24 hours

Figure 19. Observation of cell internalization in liver using TEM

TEM image of liver tissue, which was collected at different time points (5 min, 1 hour, 4 hours, and 24 hours) after administration of ^{64}Cu-ESIONs, was acquired. Uptake of ESIONs was observed from the early time point in various cells, such as Kupffer cell, hepatocyte, and liver sinusoidal endothelial cell. Red arrow indicates internalized ESIONs clustered inside the intracellular vesicles, including endosomes and lysosome. Blue arrow indicates pinocytosis observed in the endothelial cells, which is assumed to be the cell internalization mechanism of ESIONs.

Part 3. Monitoring microscopic distribution of radiolabeled ESIONs in vivo

PET/MRI image was obtained in the mouse tumor model, 4 hours after intratumoral injection of radiolabeled ESIONs. Compared to the pre-scan, the 3D T1-weighted GRE MRI scan at 4 hours showed a bright signal in the tumor, and PET derived radioactivity was observed on the corresponding site (Figure 20a). TEM image revealed that radiolabeled ESIONs were mostly located at the extracellular space, as a freely dispersed form (Figure 20b).
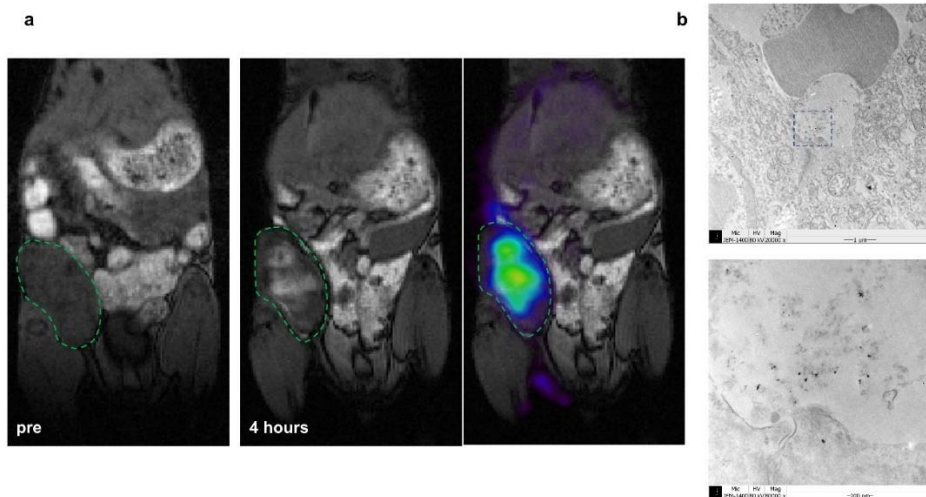
Figure 20. Monitoring of microscopic distribution in tumor model

a, Coronal image of PET/MRI was acquired from the mouse tumor model, 4 hours after intratumoral injection of ^{64}Cu-ESIONs. **b,** Corresponding TEM image was obtained to visualize the microscopic distribution of ^{64}Cu-ESIONs.

Discussion

Biodistribution and pharmacokinetics of micelle encapsulated ESIONs were evaluated after radiolabeling. The radiolabeling process did not induce significant changes in characteristics of micelle encapsulated ESIONs and when considering the in vitro and in vivo stability, radioactivity seemed to well reflect the in vivo dynamic of micelle encapsulated ESIONs. the biodistribution study of radiolabeled ESIONs revealed a relatively long blood circulation time. While maintaining their intact radiolabeling form, radiolabeled ESIONs were mainly cleared through the hepatobiliary pathway and up to 40% of injected ^{64}Cu-ESIONs were excreted within 24 hours. I investigated the difference between PET and MRI signal in vivo, using simultaneous PET/MRI. Both the in vivo and phantom study, the signal intensity of the blood pool in 3D T1-weighted GRE MRI was found to have a concentration-dependent change in the low concentration range, but it was considered non-linear in the high concentration range. Meanwhile, ^{64}Cu induced radioactivity showed excellent linearity with the concentration. Next, 3D T1-weighted GRE induced MRI signal showed a linear relationship with cell internalization, which was reflected by the retention fraction, in the liver. Using this result, potential usage of radiolabeled ESIONs for monitoring microscopic distribution was evaluated in the mouse tumor model.

Inorganic nanoparticles, including IONPs, can be taken up by the reticuloendothelial system (RES) and remain in the corresponding organs, which may consequently, lead to toxicological side effects. The mechanism by which nanoparticles exhibits cytotoxicity has not been clearly elucidated, but it is hypothesized that nanoparticles produce reactive oxygen species (ROS) and as a

result induce cellular oxidative stress (57). IONPs, with their excellent biocompatibility, is considered as a safe and non-toxic nanoparticle. Studies have been conducted, since the first clinical administration decades ago, to confirm the side effects of IONPs after administration to humans (58-60). From the studies, overall adverse events were reported to occur between 5% and 24%, mostly mild to moderate adverse events, and serious adverse events were observed only in a very limited number of patients. A recent Ferumoxytol study in 8666 patients with iron deficiency, reported a 1.25% overall incidence of side effects and a serious side effect of 0.21% (61). However, there are still concerns about the lack of clear results on long-term side effects (62). Moreover, conflicting evidence regarding toxicity has been reported based on in vitro and in vivo studies (29, 63-69). This is, for some reason, because the IONPs used in each experiment were conducted using IONPs with various sizes, shapes, surface charge, surface coating materials, concentration and different in vitro and in vivo models. Thus, when applying a new particle with different sizes, surface encapsulation method, or targeting ligand, a systematic toxicity study is additionally needed, which can be supported by biodistribution and pharmacokinetic studies. However, for this novel micelle encapsulated ESIONs, biodistribution and pharmacokinetic studies are limited to date which are prerequisite for the clinical translation.

From the biodistribution and pharmacokinetic study, I have observed relatively long blood circulation, approximately 62 min at the early time point and 12.8 hours at a later period, and rapid hepatobiliary excretion, up to 40% at 24 hours. In general, nanoparticles, after in vivo administration, are cleared through three main mechanisms, which are renal system, hepatobiliary systems, and RES (70, 71). Each mechanism has a different clearance time. Nanoparticles can be

cleared through the renal system within hours to days, and through the hepatobiliary system within hours to weeks, whereas, nanoparticles, retained in the RES, can be eliminated after degradation which takes months to years. Various factors such as size, surface coating, surface charge, and shape are involved in blood clearance and excretion of nanoparticles.

Size is the initial key factor in determining the main clearance pathway of the nanoparticle. A quantum dot study revealed that effective excretion through the urinary system can be achieved at the hydrodynamic size less than 5.5 nm, the renal filtration cutoff size (72). Bawendi et al. reported exceedingly small IONPs with a hydrodynamic size of 4.7 nm (32). They used IONP with a core size of 3 nm and zwitterionic dopamine sulfonate for the ultrathin hydrophilic shell. Due to its small size, the IONP in the study showed effective T1 contrast and rapid clearance through the renal system. As a result, it showed relatively fast blood clearance, half-life of 19 min. Still, it is a long blood half-life compared to a common Gd-DTPA agent (2 min), but it may not be a sufficiently long time for steady-state imaging and tumor imaging. Nanoparticles exceeding the diameter of liver sinusoidal fenestrae, which ranges from 50 to 200 nm, are mainly taken up by the RES and retained (70). In the same vein, large IONPs (d_H ~100-200nm) are rapidly removed from the blood pool after administration and mostly are retained in the liver and spleen after being phagocytosed by the tissue macrophage (73, 74). Generally, these large-sized IONPs have shown short blood half-life, half of the injected dose was cleared within minutes (74-77). Besides the short blood circulation time, the degradation and excretion process in the RES is significantly slow, which can take from months to years (78, 79). Prolonged retention of IONPs from this slow clearance process, may raise the concerns for long-term toxicity.

Nanoparticle with size ranging from 8 nm to 50 nm can pass through the liver fenestrae extravasate into the space of Disse and directly interact with the hepatocyte (70, 80). Subsequently, the nanoparticle can be endocytosed into the hepatocyte, then released through the bile canaliculi, and finally excreted through the intestine. In this size range, rapid excretion through the kidneys can also be avoided. Various biodistribution studies using USPIO, with a focus on FDA approved ferumoxytol (d_H ~30 nm) and ferumoxtran-10 (d_H ~30 nm), have been conducted. Both ferumoxytol and ferumoxtran-10 showed prolonged blood circulation with blood half-life estimated to be 12 hours and 30 hours, respectively (81, 82). In the animal models, the blood half-life is relatively shorter (78), as ferumoxytol showing blood half-life of approximately 45 minutes in the mice (83). Although it has the advantage of long circulation time, there still is a concern for systemic clearance of the IONPs in vivo. Preclinical study of Ferumoxtran-10 after ^{59}Fe labeling revealed that a considerable amount of USPIO remained in the body and only 22% was excreted in 84 days, mainly as feces (84).

The size of radiolabeled ESIONs (9.47 nm) in this study seems to be optimal as an effective blood pool imaging agent by minimizing uptake in RES such as Kupffer cells and avoiding renal clearance so that it can remain in the blood pool for a long time. The larger the size, the greater the uptake in the RES, so smaller particles can avoid prolonged retention in the macrophage (70, 85), as a result, a larger portion can pass through the hepatocyte and excrete into the hepatobiliary. Also, by minimizing toxicity through rapid hepatobiliary excretion, radiolabeled ESIONs are expected that there may be fewer concerns about safety issues.

Another important factor affecting the clearance pathway is the surface

coating method. Without proper surface coating, most nanoparticles tend to aggregate due to hydrophobic interactions or Van der Waals forces, then opsonization accelerates and as a result gets eliminated through the RES rapidly (86, 87). Opsonization of nanoparticle is a process whereby surface-bound opsonin, such as antibody and complement proteins, undergo a conformational change to have a stronger attraction to the receptors of the phagocytes on the particle surface (88). By minimizing opsonization, recognition by RES can be minimized, and as a result, the stealth effect can be maximized to obtain high stability, long blood pool circulation, and less RES retention of the nanoparticle. Opsonization of nanoparticles may vary depending on the surface properties, including charge and hydrophobicity, thus, it can be manipulated by the surface coating materials (89, 90). Different types of materials, including synthetic polymeric molecules, such as polyethylene glycol (PEG) (91), and natural polymers, such as dextran (92), albumin (93), have been used for surface coating. Among these polymers, dextran and PEG have been the most widely used materials for IONPs surface coating, and most of the clinically approved IONPs are coated with dextran and it's derivative (94). These surface coating has shown enhanced stability, low cytotoxicity, and longer blood circulation time (74, 94-96). In addition to the surface coating method with polymers, encapsulation methods that incorporate IONPs inside the vesicles, such as liposomes (97-99) and micelle (100), has been introduced. Like the conventional surface coating method, the encapsulation method also showed prolonged blood circulation time by minimizing RES uptake, high colloidal safety and improved biocompatibility (94). In general, it is known that surface coating can reduce cell toxicity by improving stability and reducing the number of oxidative sites (66, 101, 102). More importantly, encapsulated surface of IONPs can be further functionalized based on the terminal active groups.

Since the micelle encapsulation method was first applied to a quantum dot and proved its possibility (103), studies have been conducted to optimize this method, to be more simple and rapid, for various nanoparticles (104-106). Recently, Lee et al. integrated these progress to make a quick and straightforward one-step method for producing multifunctional nanoparticles under mild condition (39) andfurther applied for the encapsulation and radiolabeling of IONPs ($d_C \sim 5nm$, $d_H \sim 10.12nm$), to be used as a PET/MRI dual-modality agent for lymph node imaging (18). In the study micelle encapsulated radiolabeled IONPs showed no significant cellular toxicity, but, in vivo systemic effect was not evaluated, as IONPs were injected through the footpad.

Moreover, micelle encapsulation can accelerate the hepatobiliary clearance of the nanoparticles. Seo et al. reported the micelle encapsulated upconverting nanoparticles (UCNP) can be cleared via hepatobiliary excretion in their intact forms (107). They have revealed efficient hepatobiliary excretion of UCNP after initially taken up by the hepatocyte, using PET and TEM images. However, underlying molecular mechanisms are not understood well. For rapid hepatobiliary excretion, recognition by RES should be avoided. In general, for nanoparticles to be excreted through the hepatobiliary system, they must path through these steps: (a) liver sinusoid, (b) space of Disse, (c) hepatocytes, (d) bile ducts, (e) intestines, and (f) out of the body. During this process, interaction with liver non-parenchymal cells (e.g. Kupffer cells) affects excretion. Existing studies have confirmed that if MPS recognition can be effectively avoided, excretion through hepatobiliary system may increase. For example, depletion of Kupffer cells through clodronate liposomes (108), positive surface change (109), and micelle encapsulation increased excretion through the liver (107). It is speculated that micelle

encapsulation of the ESIONs may lower the recognition by RES. After avoiding recognition by RES, micelle encapsulated ESIONs must be effectively internalized into hepatocytes. Heine et al. confirmed that polymer coated nanoparticles are mainly accumulated in liver sinusoidal endothelial cells, while micelle encapsulated nanoparticles are taken up in hepatocytes and Kupffer cells (110). In the study, low-density lipoprotein (LDL) receptor knock-out transgenic mice were used. In the wild type, uptake of micelle encapsulated nanoparticles was observed in both hepatocyte and Kupffer cells, whereas in transgenic mice, uptake was observed only in the Kupffer cells. Additionally, it was confirmed that hepatocyte uptake reduction in apolipoprotein E (ApoE) deficient mice. Comprehensively it is speculated that the LDL receptor and ApoE appear to play important roles in the hepatocyte uptake of micelle encapsulated ESIONs

Various methods have been used to evaluate the biodistribution and pharmacokinetics of IONPs. A qualitative and quantitative method for the biodistribution study can be roughly categorized into ex vivo and in vivo studies (78). Simply, using an optical microscope, the distribution of IONPs can be easily confirmed by staining the extracted tissue. However, staining with Prussian Blue has an important limitation that it is difficult to distinguish between endogenous iron and exogenous IONP. The TEM image is a representative ex vivo imaging tool that has a resolution below 1 nm and, as a result, can utilize it to evaluate the microscopic distribution of IONPs (111-113). However, TEM image-based biodistribution studies have an inherent limitation, due to the small field of view it can only provide information regarding a selected area. For the quantitative biodistribution study, spectroscopy and magnetometry techniques can be used. The mass spectrometry technique that ionizes a sample using an inductively coupled

plasma is used in many ways for the accurate quantification of iron, but it also has limitations, such as the staining method, that cannot distinguish between endogenous and exogenous components. Conversely, the magnetometry technique can distinguish exogenous components using magnetic properties and allow accurate quantification (114). Ex vivo methods can observe the microscopic distribution of IONPs with high resolution and provide accurate quantitative values, but since they can be observed only after animal sacrifice, it is impossible to image the function of living organs and it is difficult to track the dynamic behavior over time.

In vivo imaging can compensate for these limitations. The optical image is frequently used for in vivo studies, which can be obtained and quantified by labeling a fluorophore on a core or surface. However, IONPs themselves may have a quenching effect on fluorescence signal (68). Moreover, weak tissue penetration limits its clinical application. Based on the superparamagnetic properties of IONPs, MRI has been the most widely used method for the evaluation of in vivo biodistribution and quantification. Recently, to overcome the inherent limitations of T2 relaxivity based quantification, studies using T1 quantitative mapping sequences, such as UTE (ultra-short echo time) and SWIFT (sweep imaging with Fourier transformation), have been reported, which can obtain linear quantitative values at relatively higher concentration range (115-117). Though, endogenous iron and background tissue interference may affect the accurate quantification in relaxivity based methods. Magnetic particle imaging (MPI) is a more recent tomographic imaging technique, it forms images by exploiting the intrinsic saturation property of IONPs (118). MPI can track and quantify nanoparticle concentrations regardless of endogenous irons and without tissue background noise.

Similarly, PET, using radiolabeled particles, can be used for tracking and quantifying only the injected IONPs without being affected by the background. Radiolabeling of the nanoparticle can be done either in the core or on the surface. Both core (32, 119-121) and surface labeling (18, 122) have been used for in vivo tracking of IONPs.

There is a concern for in vivo stability of radiolabeling, especially for surface labeled nanoparticles. A recent study has evaluated the in vivo integrity of polymer-coated gold nanoparticle with both core and surface labeling, and suggest that disassociation of nanoparticle surface coating is caused by the intracellular proteolytic enzymes (123). The disintegration of the radiolabeled nanoparticle may also occur in the blood circulation by the plasma enzyme (124). Given the high radiochemical purity in the blood and the presence of mostly disintegrated form in urine, it is speculated that radiolabeled ESIONs will be released through urine as soon as it is disassociated. Referring to the distribution of ^{64}Cu-NOTA-C$_{18}$ shown in the micelle encapsulated UCNP study (107), in this study, ^{64}Cu-NOTA, not micelle encapsulation, may disintegrate and clear through the renal system. This is in line with the previous study which evaluated the in vivo integrity of IONPs using ^{59}Fe, as core and ^{111}In as surface labeling radionuclide (125). In this study, the radioactivity of ^{59}Fe and ^{111}In showed an overall similar biodistribution pattern but showed a significant difference in the kidney, which demonstrates that the disassociated ^{111}In is mainly cleared through the renal system. Collectively, in vivo stability can be easily monitored through estimation of urinary output, but since, the urinary excretion was minimal (%ID: 4.45%, at 24 hours), the effect of disintegration in our study might be negligible. Furthermore, high radiochemical purity of stool contents demonstrates that radioactivity of ^{64}Cu well reflects the in

vivo dynamics of ESIONs.

Indeed, biodegradation was beyond the scope of this study. Although biodegradation has minimal effect in the early dynamics of radiolabeled ESIONs, it is an important factor related to long-term clearance and chronic toxicity. Commonly, it is speculated that the biodegradation of IONPs would be similar to that of ferritin, in which protein shell gets dissolved in the intracellular lysosome (78). The degradation of exogenously injected IONPs mainly takes place in the intracellular lysosome of macrophage, in different RES organs (126, 127). The study of ferumoxtran-10 revealed different elimination patterns of iron oxide core and dextran shell, using the dual-labeling method with ^{59}Fe and ^{14}C, representing the core and shell, respectively (84). After phagocytosed by the RES, the dextran shells were dissolved and were mostly eliminated through the renal system (89% in 56 days). Whereas, the iron core was cleared very slowly, mostly through the hepatobiliary system (21% in 84 days). Because of such difference in the clearance of core and shell, degradability should be considered for evaluation and quantification of long-term pharmacokinetics of radiolabeled ESIONs in the future study.

As a result of biodegradation, the free iron can trigger the production of ROS which may induce chronic toxicity (68, 128). However, the high hepatobiliary clearance shown in this study demonstrates that the uptake portion to RES, including Kupffer cell, is relatively low compared to the hepatocyte, which means that the biodegradation portion of radiolabeled ESIONs by RES is relatively small. Also, it is reported, that IONPs with small core sizes showed faster biodegradation in the liver and spleen (129). Overall, biodegradation of radiolabeled ESIONs is

expected to occur less and faster by RES, so there may be less chronic toxicity.

Micelle encapsulated ESIONs with 3 nm core size showed fair r_1 relaxivity of 3.43 mM^{-1}s^{-1} and a relatively low r_2/r_1 ratio of 5.36, proving its potential as an effective T1 contrast agent. Radiolabeling process did not significantly alter the relaxation properties of ESIONs. After in vivo administration of radiolabeled ESIONs, simultaneous PET/MRI imaging revealed high T1 contrast power along the blood pool with corresponding radioactivity. Still, when referring to studies related to Gd, which has been the most widely used T1 contrast agent, it is necessary to consider various concerns of optimization and obtaining best contrast for the clinical application of ESIONs.

Signal intensity is determined by the inherent property of the contrast agent and local tissue concentration, so theoretically, the intensity of the signal should increase as the concentration of the contrast agent increases, but in reality, obtaining the best contrast may be limited due to the T2-related signal decay. Thus, signal intensity in the T1-weighted MRI is the consequence of the trade-off between T1 related effect of increasing the contrast and T2-related effect of reducing the contrast (40). Generally, in the high concentration range, due to high T2 related effect, signal quenching is observed (40, 130, 131). Though, in the concentration range for the routine practice of Gd-based T1-weighted MRI, such a phenomenon is rarely occurring and only observed in the regions where gadolinium is highly concentrated, such as the bladder (132). However, IONP based contrast agents, with stronger magnetic properties than gadolinium, have stronger T2 shortening effect and as a result, may show considerable signal quenching in the clinical dosage. Phantom study of USPIO revealed signal

decrease at a concentration higher than 0.2 mM in the 3D T1-weighted GRE sequence (117).

In this study, radiolabeled ESIONs showed a similar pattern of non-linearity and reduce of T1 signal intensity in the high concentration range. Whereas, radioactivity showed a linear correlation over the entire concentration range. In vivo image revealed that the time-dependent signal intensity change appeared in various patterns at different concentrations. Linear signal decay in the blood pool was only observed when low concentration (2.5 mgFe/kg) of ESIONs was injected. Conversely, signal plateau and even reduced signal were observed, when medium concentration (5 mgFe/kg) and high concentration (10 mgFe/kg) of ESIONs were injected, respectively. Thus, for accurate quantification, using MRI signal intensity, it would be better to administer a low concentration of ESIONs. And for the purpose to maintain enhanced signal in the blood pool for a longer period, a higher concentration may be optimal. Moreover, when applying radiolabeled ESIONs with medium concentration (5 mgFe/kg), the best contrast of the blood pool signal can be maintained for a long time, and at the same time, accurate quantitation using radioactivity may also be possible. Nevertheless, it is necessary to consider the trade-off between high concentration-induced toxicity and achieving the best contrast.

Signal intensity can also be affected by the local distribution of contrast agents. When the local distribution of contrast agents changes from a freely dispersed to clustered state or when contrast agents internalize into the cell, reduction of T1 relaxation occurs and may induce signal intensity quenching in T1-weighted MRI (42-44, 133). Phagocytosis and pinocytosis are the major cell internalization

76

mechanism of nanoparticles. Large IONPs ($d_H > 100nm$) are phagocytosed by the RES, while, small IONPs ($d_H < 20nm$) are internalized mainly through pinocytosis, non-specific and non-receptor mediated endocytosis (73, 134). Through either mechanism, cell internalized nanoparticles mostly end-up in the lysosome and are clustered (135). The signal quenching, after cell internalization, may be the consequence of r_1 reduction due to limited water exchange inside the vesicles or strengthening of the T2 shortening effect due to high local concentration and aggregation (33, 133).

As expected, signal quenching was observed in the liver over time, while radioactivity remained relatively constant. Since the liver is the organ where most nanoparticles accumulate or path through, radiolabeled ESIONs may have been accumulated in the liver RES, including Kupffer cell, liver sinusoidal endothelial cells and also in the hepatocyte. TEM images complement the result that from early time point (5 min), radiolabeled ESIONs were internalized into the cells.

Although signal quenching after cell internalization can limit accurate quantification, various clinical applications may be possible. Aghighi et al. proposed a strategy to image tumor necrosis from the speculation that administered USPIO may be freely dispersed in the tumor necrosis, while internalized and clustered in the tumor tissue, resulting in a different T1/T2 enhancement pattern (136). Girard et al. focused on this issue and proposed that combining the relaxation-based mapping technique and magnetic susceptibility mapping, which can provide a quantitative value of IONPs concentration regardless of microscopic distribution, can provide a robust quantitative value of internalized faction and their local concentration (42). Moreover, it is speculated that microscopic distribution

can be simply quantified using radiolabeled ESIONs. As shown from the liver washout model, MRI signal intensity can provide an estimation of tissue retention fraction and at the same time, total tissue concentration of radiolabeled ESIONs can be quantified using radioactivity measured by PET.

Magnetic hyperthermia, which is generated when intratumorally injected IONPs are exposed to an altering external magnetic field, can be a promising therapeutic tool for cancer treatment (2, 3, 137). The specific absorption rate (SAR), indicating the heating potential of the administered particle, is the major factor in determining the dosage (3). Furthermore, it is important to accurately assess the tumor uptake to evaluate whether the correct dose has been directed to the target tumor site. However, currently available methods using MRI and CT scan has limitations (138). Also, it cannot distinguish the IONPs' local distribution, whether it is internalized in the cell or it is freely distributed in the extracellular space (138). Such an internalized portion is important as the nanoparticle internalizes, it aggregates and the SAR can grow up (139). Thus, it may be possible to more accurately predict the therapeutic effect by radioactivity-based quantification of tumor uptake and estimating the microscopic distribution using radiolabeled ESIONs.

Radiolabeled ESIONs may also reveal the immune status in the tumor microenvironment (TME). Recently, the paradigm of cancer treatment is changing from the cytotoxic chemotherapy attacking the cancer itself to an immunotherapy agent that induces cancer attack by activating the body's immune system (140). Among them, the immune checkpoint inhibitor has proven its potential with an effective and persistent therapeutic effect. However, there are still concerns, such

as limited efficacy in some patients and resistance in most common cancers. Accordingly, studies are being conducted, with a focus on the impact of TME on the efficacy of immunotherapy and the immune evasion mechanism of cancer, in order to turn immunologically "cold" tumor into a "hot" tumor (141, 142). The "cold" tumor has characteristics of reduced tumor antigens, antigen-presenting cell deficit, and absence of T cell activation, whereas, "hot" tumors have abundant lymphocyte infiltration in the TME. From the previous studies, it is reported that IONPs are more preferred by the immune cells compared with the tumor cells (143, 144). Comprehensively, "cold" and "hot" tumors may show different enhancement pattern by radiolabeled ESIONs, as former showing bright signal owing to less cell uptake by tumoral immune cells and latter showing relatively dark signal. In this study, 4 hours after intratumoral administration of radiolabeled ESIONs, positive enhancement was observed at the tumor with corresponding radioactivity, indicating the tumor may be immunologically "cold". Indeed, breast cancers exhibit relatively low immune cell infiltration, thus, have been considered as "cold" tumor (145). This also applies to the mouse 4T1 breast tumor model (146), which was used in this study.

Conclusion

In conclusion, the in vivo dynamic of micelle encapsulated ESIONs was evaluated using simultaneous PET/MRI. Micelle encapsulated ESIONs can be an effective T1 contrast agent with relatively long blood circulation time and rapid excretion through the hepatobiliary system, which offers both efficiency and safety. Additionally, by complementing strengths and weaknesses of PET and MRI, radiolabeled ESIONs can be a promising multimodal imaging agent for monitoring microscopic distribution in vivo.

REFERENCES

1.   Kim BY, Rutka JT, Chan WC. Nanomedicine. N Engl J Med. 2010;363(25):2434-43.

2.   Kandasamy G, Maity D. Recent advances in superparamagnetic iron oxide nanoparticles (SPIONs) for in vitro and in vivo cancer nanotheranostics. Int J Pharm. 2015;496(2):191-218.

3.   Hilger I. In vivo applications of magnetic nanoparticle hyperthermia. Int J Hyperthermia. 2013;29(8):828-34.

4.   Jordan A, Wust P, Fahling H, John W, Hinz A, Felix R. Inductive heating of ferrimagnetic particles and magnetic fluids: physical evaluation of their potential for hyperthermia. Int J Hyperthermia. 1993;9(1):51-68.

5.   Chertok B, Moffat BA, David AE, Yu F, Bergemann C, Ross BD, et al. Iron oxide nanoparticles as a drug delivery vehicle for MRI monitored magnetic targeting of brain tumors. Biomaterials. 2008;29(4):487-96.

6.   Mahmoudi M, Sant S, Wang B, Laurent S, Sen T. Superparamagnetic iron oxide nanoparticles (SPIONs): development, surface modification and applications in chemotherapy. Adv Drug Deliv Rev. 2011;63(1-2):24-46.

7.   Li L, Jiang W, Luo K, Song H, Lan F, Wu Y, et al. Superparamagnetic iron oxide nanoparticles as MRI contrast agents for non-invasive stem cell labeling and tracking. Theranostics. 2013;3(8):595-615.

8.   Lee N, Kim H, Choi SH, Park M, Kim D, Kim HC, et al. Magnetosome-like ferrimagnetic iron oxide nanocubes for highly sensitive MRI of single cells and transplanted pancreatic islets. Proc Natl Acad Sci U S A. 2011;108(7):2662-7.

9.   Weissleder R, Elizondo G, Wittenberg J, Rabito CA, Bengele HH, Josephson L. Ultrasmall superparamagnetic iron oxide: characterization of a new class of contrast agents for MR imaging. Radiology. 1990;175(2):489-93.

10.   Thorek DL, Chen AK, Czupryna J, Tsourkas A. Superparamagnetic iron oxide nanoparticle probes for molecular imaging. Ann Biomed Eng. 2006;34(1):23-38.

11.   Wang YX. Superparamagnetic iron oxide based MRI contrast agents: Current status of clinical application. Quant Imaging Med Surg. 2011;1(1):35-40.

12.   Pouliquen D, Perdrisot R, Ermias A, Akoka S, Jallet P, Le Jeune JJ. Superparamagnetic iron oxide nanoparticles as a liver MRI contrast agent: contribution of microencapsulation to improved biodistribution. Magn Reson Imaging. 1989;7(6):619-27.

13.   Corot C, Robert P, Idee JM, Port M. Recent advances in iron oxide nanocrystal technology for medical imaging. Adv Drug Deliv Rev. 2006;58(14):1471-504.

14.   Ros PR, Freeny PC, Harms SE, Seltzer SE, Davis PL, Chan TW, et al. Hepatic MR imaging with ferumoxides: a multicenter clinical trial of the safety and efficacy in the detection of focal hepatic lesions. Radiology. 1995;196(2):481-8.

15.   Yoo RE, Choi SH, Cho HR, Jeon BS, Kwon E, Kim EG, et al. Magnetic resonance imaging diagnosis of metastatic lymph nodes in a rabbit model: efficacy of PJY10, a new ultrasmall superparamagnetic iron oxide agent, with monodisperse iron oxide core and multiple-interaction ligands. PLoS One. 2014;9(9):e107583.

16.   Weissleder R, Elizondo G, Wittenberg J, Lee AS, Josephson L, Brady TJ. Ultrasmall superparamagnetic iron oxide: an intravenous contrast agent for assessing lymph nodes with MR imaging. Radiology. 1990;175(2):494-8.

17.   Pultrum BB, van der Jagt EJ, van Westreenen HL, van Dullemen HM, Kappert P, Groen H, et al. Detection of lymph node metastases with ultrasmall superparamagnetic iron oxide (USPIO)-enhanced magnetic resonance imaging in oesophageal cancer: a feasibility study. Cancer Imaging. 2009;9:19-28.

18.   Yang BY, Moon SH, Seelam SR, Jeon MJ, Lee YS, Lee DS, et al. Development of a multimodal imaging probe by encapsulating iron oxide nanoparticles with functionalized amphiphiles for lymph node imaging. Nanomedicine (Lond). 2015;10(12):1899-910.

19.   Trivedi RA, Mallawarachi C, JM UK-I, Graves MJ, Horsley J, Goddard MJ, et al. Identifying inflamed carotid plaques using in vivo USPIO-enhanced MR imaging to label plaque macrophages. Arterioscler Thromb Vasc Biol. 2006;26(7):1601-6.

20.   Dousset V, Delalande C, Ballarino L, Quesson B, Seilhan D, Coussemacq M, et al. In vivo macrophage activity imaging in the central nervous system detected by magnetic resonance. Magn Reson Med. 1999;41(2):329-33.

21.   Corot C, Petry KG, Trivedi R, Saleh A, Jonkmanns C, Le Bas JF, et al. Macrophage imaging in central nervous system and in carotid atherosclerotic plaque using ultrasmall superparamagnetic iron oxide in magnetic resonance imaging. Invest Radiol. 2004;39(10):619-25.

22.   Kim BH, Lee N, Kim H, An K, Park YI, Choi Y, et al. Large-scale synthesis of uniform and extremely small-sized iron oxide nanoparticles for high-resolution T1 magnetic resonance imaging contrast agents. J Am Chem Soc. 2011;133(32):12624-31.

23.   Lu Y, Xu YJ, Zhang GB, Ling D, Wang MQ, Zhou Y, et al. Iron oxide nanoclusters for T 1 magnetic resonance imaging of non-human primates. Nat Biomed Eng. 2017;1(8):637-43.

24.	Anselmo AC, Mitragotri S. A Review of Clinical Translation of Inorganic Nanoparticles. AAPS J. 2015;17(5):1041-54.

25.	Caravan P. Strategies for increasing the sensitivity of gadolinium based MRI contrast agents. Chem Soc Rev. 2006;35(6):512-23.

26.	Barker PB, Lin DDM, Mahesh M. Retention Concerns About MR Studies Using Gadolinium-Based Contrast Agents. J Am Coll Radiol. 2018;15(6):934-6.

27.	Kanal E. Gadolinium based contrast agents (GBCA): Safety overview after 3 decades of clinical experience. Magn Reson Imaging. 2016;34(10):1341-5.

28.	Kanda T, Ishii K, Kawaguchi H, Kitajima K, Takenaka D. High signal intensity in the dentate nucleus and globus pallidus on unenhanced T1-weighted MR images: relationship with increasing cumulative dose of a gadolinium-based contrast material. Radiology. 2014;270(3):834-41.

29.	Lee N, Hyeon T. Designed synthesis of uniformly sized iron oxide nanoparticles for efficient magnetic resonance imaging contrast agents. Chem Soc Rev. 2012;41(7):2575-89.

30.	Tromsdorf UI, Bruns OT, Salmen SC, Beisiegel U, Weller H. A highly effective, nontoxic T1 MR contrast agent based on ultrasmall PEGylated iron oxide nanoparticles. Nano Lett. 2009;9(12):4434-40.

31.	Hu F, Jia Q, Li Y, Gao M. Facile synthesis of ultrasmall PEGylated iron oxide nanoparticles for dual-contrast T1- and T2-weighted magnetic resonance imaging. Nanotechnology. 2011;22(24):245604.

32.	Wei H, Bruns OT, Kaul MG, Hansen EC, Barch M, Wisniowska A, et al. Exceedingly small iron oxide nanoparticles as positive MRI contrast agents. Proc Natl Acad Sci U S A. 2017;114(9):2325-30.

33.   Bao Y, Sherwood J, Sun Z. Magnetic iron oxide nanoparticles as T 1 contrast agents for magnetic resonance imaging. Journal of materials chemistry C. 2018;6(6):1280-90.

34.   Loubeyre P, Zhao S, Canet E, Abidi H, Benderbous S, Revel D. Ultrasmall superparamagnetic iron oxide particles (AMI 227) as a blood pool contrast agent for MR angiography: experimental study in rabbits. J Magn Reson Imaging. 1997;7(6):958-62.

35.   Anzai Y, Prince MR, Chenevert TL, Maki JH, Londy F, London M, et al. MR angiography with an ultrasmall superparamagnetic iron oxide blood pool agent. J Magn Reson Imaging. 1997;7(1):209-14.

36.   Ahlstrom KH, Johansson LO, Rodenburg JB, Ragnarsson AS, Akeson P, Borseth A. Pulmonary MR angiography with ultrasmall superparamagnetic iron oxide particles as a blood pool agent and a navigator echo for respiratory gating: pilot study. Radiology. 1999;211(3):865-9.

37.   Shen Z, Wu A, Chen X. Iron Oxide Nanoparticle Based Contrast Agents for Magnetic Resonance Imaging. Mol Pharm. 2017;14(5):1352-64.

38.   Hajiw S, Schmitt J, Imperor-Clerc M, Pansu B. Solvent-driven interactions between hydrophobically-coated nanoparticles. Soft matter. 2015;11(19):3920-6.

39.   Lee YK, Jeong JM, Hoigebazar L, Yang BY, Lee YS, Lee BC, et al. Nanoparticles modified by encapsulation of ligands with a long alkyl chain to affect multispecific and multimodal imaging. J Nucl Med. 2012;53(9):1462-70.

40.   Hagberg GE, Scheffler K. Effect of r(1) and r(2) relaxivity of gadolinium-based contrast agents on the T(1)-weighted MR signal at increasing magnetic field strengths. Contrast Media Mol Imaging. 2013;8(6):456-65.

41.   Nazarpoor M, Poureisa M, Daghighi MH. Comparison of maximum signal intensity of contrast agent on t1-weighted images using spin echo, fast spin echo and inversion recovery sequences. Iran J Radiol. 2012;10(1):27-32.

42.   Girard OM, Ramirez R, McCarty S, Mattrey RF. Toward absolute quantification of iron oxide nanoparticles as well as cell internalized fraction using multiparametric MRI. Contrast Media Mol Imaging. 2012;7(4):411-7.

43.   Klug G, Kampf T, Bloemer S, Bremicker J, Ziener CH, Heymer A, et al. Intracellular and extracellular T1 and T2 relaxivities of magneto-optical nanoparticles at experimental high fields. Magn Reson Med. 2010;64(6):1607-15.

44.   Terreno E, Geninatti Crich S, Belfiore S, Biancone L, Cabella C, Esposito G, et al. Effect of the intracellular localization of a Gd-based imaging probe on the relaxation enhancement of water protons. Magn Reson Med. 2006;55(3):491-7.

45.   Lee DS. Radionanomedicine: Springer International Publishing 2018.

46.   Choi H, Lee YS, Hwang DW, Lee DS. Translational radionanomedicine: a clinical perspective. Eur J Nanomed. 2016;8(2):71-84.

47.   Tichauer KM, Wang Y, Pogue BW, Liu JT. Quantitative in vivo cell-surface receptor imaging in oncology: kinetic modeling and paired-agent principles from nuclear medicine and optical imaging. Phys Med Biol. 2015;60(14):R239-69.

48.   Mannheim JG, Schmid AM, Schwenck J, Katiyar P, Herfert K, Pichler BJ, et al. PET/MRI Hybrid Systems. Semin Nucl Med. 2018;48(4):332-47.

49.   Ko GB, Yoon HS, Kim KY, Lee MS, Yang BY, Jeong JM, et al. Simultaneous Multiparametric PET/MRI with Silicon Photomultiplier PET and Ultra-High-Field MRI for Small-Animal Imaging. J Nucl Med. 2016;57(8):1309-15.

50. Ko GB, Kim KY, Yoon HS, Lee MS, Son JW, Im HJ, et al. Evaluation of a silicon photomultiplier PET insert for simultaneous PET and MR imaging. Med Phys. 2016;43(1):72.

51. Xie J, Chen K, Huang J, Lee S, Wang J, Gao J, et al. PET/NIRF/MRI triple functional iron oxide nanoparticles. Biomaterials. 2010;31(11):3016-22.

52. Yang X, Hong H, Grailer JJ, Rowland IJ, Javadi A, Hurley SA, et al. cRGD-functionalized, DOX-conjugated, and (6)(4)Cu-labeled superparamagnetic iron oxide nanoparticles for targeted anticancer drug delivery and PET/MR imaging. Biomaterials. 2011;32(17):4151-60.

53. Son JW, Kim KY, Park JY, Kim K, Lee YS, Ko GB, et al. SimPET: a Preclinical PET Insert for Simultaneous PET/MR Imaging. Mol Imaging Biol. 2020.

54. Park J, An K, Hwang Y, Park JG, Noh HJ, Kim JY, et al. Ultra-large-scale syntheses of monodisperse nanocrystals. Nat Mater. 2004;3(12):891-5.

55. Liu X, Chen Y, Li H, Huang N, Jin Q, Ren K, et al. Enhanced retention and cellular uptake of nanoparticles in tumors by controlling their aggregation behavior. ACS Nano. 2013;7(7):6244-57.

56. Shen Z, Baker W, Ye H, Li Y. pH-Dependent aggregation and pH-independent cell membrane adhesion of monolayer-protected mixed charged gold nanoparticles. Nanoscale. 2019;11(15):7371-85.

57. Apopa PL, Qian Y, Shao R, Guo NL, Schwegler-Berry D, Pacurari M, et al. Iron oxide nanoparticles induce human microvascular endothelial cell permeability through reactive oxygen species production and microtubule remodeling. Part Fibre Toxicol. 2009;6:1.

58.   Bernd H, De Kerviler E, Gaillard S, Bonnemain B. Safety and tolerability of ultrasmall superparamagnetic iron oxide contrast agent: comprehensive analysis of a clinical development program. Invest Radiol. 2009;44(6):336-42.

59.   McCormack PL. Ferumoxytol: in iron deficiency anaemia in adults with chronic kidney disease. Drugs. 2012;72(15):2013-22.

60.   Auerbach M, Pappadakis JA, Bahrain H, Auerbach SA, Ballard H, Dahl NV. Safety and efficacy of rapidly administered (one hour) one gram of low molecular weight iron dextran (INFeD) for the treatment of iron deficient anemia. Am J Hematol. 2011;86(10):860-2.

61.   Schiller B, Bhat P, Sharma A. Safety and effectiveness of ferumoxytol in hemodialysis patients at 3 dialysis chains in the United States over a 12-month period. Clin Ther. 2014;36(1):70-83.

62.   Pai AB, Garba AO. Ferumoxytol: a silver lining in the treatment of anemia of chronic kidney disease or another dark cloud? J Blood Med. 2012;3:77-85.

63.   Mahmoudi M, Hofmann H, Rothen-Rutishauser B, Petri-Fink A. Assessing the in vitro and in vivo toxicity of superparamagnetic iron oxide nanoparticles. Chem Rev. 2012;112(4):2323-38.

64.   Bellusci M, La Barbera A, Padella F, Mancuso M, Pasquo A, Grollino MG, et al. Biodistribution and acute toxicity of a nanofluid containing manganese iron oxide nanoparticles produced by a mechanochemical process. Int J Nanomedicine. 2014;9:1919-29.

65.   Naqvi S, Samim M, Abdin M, Ahmed FJ, Maitra A, Prashant C, et al. Concentration-dependent toxicity of iron oxide nanoparticles mediated by increased oxidative stress. Int J Nanomedicine. 2010;5:983-9.

66.   Park YC, Smith JB, Pham T, Whitaker RD, Sucato CA, Hamilton JA, et al. Effect of PEG molecular weight on stability, T(2) contrast, cytotoxicity, and cellular uptake of superparamagnetic iron oxide nanoparticles (SPIONs). Colloids Surf B Biointerfaces. 2014;119:106-14.

67.   Sadeghi L, Tanwir F, Yousefi Babadi V. In vitro toxity of iron oxide nanoparticle: oxidative damages on Hep G2 cells. Exp Toxicol Pathol. 2015;67(2):197-203.

68.   Patil US, Adireddy S, Jaiswal A, Mandava S, Lee BR, Chrisey DB. In Vitro/In Vivo Toxicity Evaluation and Quantification of Iron Oxide Nanoparticles. Int J Mol Sci. 2015;16(10):24417-50.

69.   Ghasempour S, Shokrgozar MA, Ghasempour R, Alipour M. Investigating the cytotoxicity of iron oxide nanoparticles in in vivo and in vitro studies. Exp Toxicol Pathol. 2015;67(10):509-15.

70.   Zhang YN, Poon W, Tavares AJ, McGilvray ID, Chan WCW. Nanoparticle-liver interactions: Cellular uptake and hepatobiliary elimination. J Control Release. 2016;240:332-48.

71.   Yu M, Zheng J. Clearance Pathways and Tumor Targeting of Imaging Nanoparticles. ACS Nano. 2015;9(7):6655-74.

72.   Choi HS, Liu W, Misra P, Tanaka E, Zimmer JP, Itty Ipe B, et al. Renal clearance of quantum dots. Nat Biotechnol. 2007;25(10):1165-70.

73.   Wang YX, Hussain SM, Krestin GP. Superparamagnetic iron oxide contrast agents: physicochemical characteristics and applications in MR imaging. Eur Radiol. 2001;11(11):2319-31.

74.   Roohi F, Lohrke J, Ide A, Schutz G, Dassler K. Studying the effect of particle size and coating type on the blood kinetics of superparamagnetic iron oxide nanoparticles. Int J Nanomedicine. 2012;7:4447-58.

75.   Lind K, Kresse M, Debus NP, Muller RH. A novel formulation for superparamagnetic iron oxide (SPIO) particles enhancing MR lymphography: comparison of physicochemical properties and the in vivo behaviour. J Drug Target. 2002;10(3):221-30.

76.   Haegele J, Duschka RL, Graeser M, Schaecke C, Panagiotopoulos N, Ludtke-Buzug K, et al. Magnetic particle imaging: kinetics of the intravascular signal in vivo. Int J Nanomedicine. 2014;9:4203-9.

77.   Arami H, Khandhar AP, Tomitaka A, Yu E, Goodwill PW, Conolly SM, et al. In vivo multimodal magnetic particle imaging (MPI) with tailored magneto/optical contrast agents. Biomaterials. 2015;52:251-61.

78.   Arami H, Khandhar A, Liggitt D, Krishnan KM. In vivo delivery, pharmacokinetics, biodistribution and toxicity of iron oxide nanoparticles. Chem Soc Rev. 2015;44(23):8576-607.

79.   Weissleder R, Stark DD, Engelstad BL, Bacon BR, Compton CC, White DL, et al. Superparamagnetic iron oxide: pharmacokinetics and toxicity. AJR Am J Roentgenol. 1989;152(1):167-73.

80.   Gaumet M, Vargas A, Gurny R, Delie F. Nanoparticles for drug delivery: the need for precision in reporting particle size parameters. Eur J Pharm Biopharm. 2008;69(1):1-9.

81.   Kooi ME, Cappendijk VC, Cleutjens KB, Kessels AG, Kitslaar PJ, Borgers M, et al. Accumulation of ultrasmall superparamagnetic particles of iron oxide in human atherosclerotic plaques can be detected by in vivo magnetic resonance imaging. Circulation. 2003;107(19):2453-8.

82.   Christen T, Ni W, Qiu D, Schmiedeskamp H, Bammer R, Moseley M, et al. High-resolution cerebral blood volume imaging in humans using the blood pool contrast agent ferumoxytol. Magn Reson Med. 2013;70(3):705-10.

83.   Harms C, Datwyler AL, Wiekhorst F, Trahms L, Lindquist R, Schellenberger E, et al. Certain types of iron oxide nanoparticles are not suited to passively target inflammatory cells that infiltrate the brain in response to stroke. J Cereb Blood Flow Metab. 2013;33(5):e1-9.

84.   Bourrinet P, Bengele HH, Bonnemain B, Dencausse A, Idee JM, Jacobs PM, et al. Preclinical safety and pharmacokinetic profile of ferumoxtran-10, an ultrasmall superparamagnetic iron oxide magnetic resonance contrast agent. Invest Radiol. 2006;41(3):313-24.

85.   Lunov O, Zablotskii V, Syrovets T, Rocker C, Tron K, Nienhaus GU, et al. Modeling receptor-mediated endocytosis of polymer-functionalized iron oxide nanoparticles by human macrophages. Biomaterials. 2011;32(2):547-55.

86.   Muthiah M, Park IK, Cho CS. Surface modification of iron oxide nanoparticles by biocompatible polymers for tissue imaging and targeting. Biotechnology advances. 2013;31(8):1224-36.

87.   Nie S. Understanding and overcoming major barriers in cancer nanomedicine. Nanomedicine (London, England). 2010;5(4):523-8.

88.   Frank MM, Fries LF. The role of complement in inflammation and phagocytosis. Immunol Today. 1991;12(9):322-6.

89.   Gessner A, Lieske A, Paulke B, Muller R. Influence of surface charge density on protein adsorption on polymeric nanoparticles: analysis by two-dimensional electrophoresis. Eur J Pharm Biopharm. 2002;54(2):165-70.

90.   Vonarbourg A, Passirani C, Saulnier P, Benoit JP. Parameters influencing the stealthiness of colloidal drug delivery systems. Biomaterials. 2006;27(24):4356-73.

91.   D'Souza A A, Shegokar R. Polyethylene glycol (PEG): a versatile polymer for pharmaceutical applications. Expert Opin Drug Deliv. 2016;13(9):1257-75.

92.   Simberg D, Park JH, Karmali PP, Zhang WM, Merkulov S, McCrae K, et al. Differential proteomics analysis of the surface heterogeneity of dextran iron oxide nanoparticles and the implications for their in vivo clearance. Biomaterials. 2009;30(23-24):3926-33.

93.   Xie J, Wang J, Niu G, Huang J, Chen K, Li X, et al. Human serum albumin coated iron oxide nanoparticles for efficient cell labeling. Chem Commun (Camb). 2010;46(3):433-5.

94.   Dadfar SM, Roemhild K, Drude NI, von Stillfried S, Knuchel R, Kiessling F, et al. Iron oxide nanoparticles: Diagnostic, therapeutic and theranostic applications. Adv Drug Deliv Rev. 2019;138:302-25.

95.   Yu M, Huang S, Yu KJ, Clyne AM. Dextran and polymer polyethylene glycol (PEG) coating reduce both 5 and 30 nm iron oxide nanoparticle cytotoxicity in 2D and 3D cell culture. Int J Mol Sci. 2012;13(5):5554-70.

96.   Remya NS, Syama S, Sabareeswaran A, Mohanan PV. Toxicity, toxicokinetics and biodistribution of dextran stabilized Iron oxide Nanoparticles for biomedical applications. Int J Pharm. 2016;511(1):586-98.

97.   Liao Z, Wang H, Lv R, Zhao P, Sun X, Wang S, et al. Polymeric liposomes-coated superparamagnetic iron oxide nanoparticles as contrast agent for targeted magnetic resonance imaging of cancer cells. Langmuir. 2011;27(6):3100-5.

98.   Nappini S, Bombelli FB, Bonini M, Nordèn B, Baglioni PJSM. Magnetoliposomes for controlled drug release in the presence of low-frequency magnetic field. 2010;6(1):154-62.

99.   Fortin-Ripoche JP, Martina MS, Gazeau F, Menager C, Wilhelm C, Bacri JC, et al. Magnetic targeting of magnetoliposomes to solid tumors with MR imaging monitoring in mice: feasibility. Radiology. 2006;239(2):415-24.

100.   Nasongkla N, Bey E, Ren J, Ai H, Khemtong C, Guthi JS, et al. Multifunctional polymeric micelles as cancer-targeted, MRI-ultrasensitive drug delivery systems. Nano Lett. 2006;6(11):2427-30.

101.   Silva AH, Lima E, Jr., Mansilla MV, Zysler RD, Troiani H, Pisciotti MLM, et al. Superparamagnetic iron-oxide nanoparticles mPEG350- and mPEG2000-coated: cell uptake and biocompatibility evaluation. Nanomedicine. 2016;12(4):909-19.

102.   Malvindi MA, De Matteis V, Galeone A, Brunetti V, Anyfantis GC, Athanassiou A, et al. Toxicity assessment of silica coated iron oxide nanoparticles and biocompatibility improvement by surface engineering. PLoS One. 2014;9(1):e85835.

103.   Dubertret B, Skourides P, Norris DJ, Noireaux V, Brivanlou AH, Libchaber A. In vivo imaging of quantum dots encapsulated in phospholipid micelles. Science. 2002;298(5599):1759-62.

104.   Fan H, Yang K, Boye DM, Sigmon T, Malloy KJ, Xu H, et al. Self-assembly of ordered, robust, three-dimensional gold nanocrystal/silica arrays. Science. 2004;304(5670):567-71.

105.   Fan H, Leve EW, Scullin C, Gabaldon J, Tallant D, Bunge S, et al. Surfactant-assisted synthesis of water-soluble and biocompatible semiconductor quantum dot micelles. Nano Lett. 2005;5(4):645-8.

106.   Carion O, Mahler B, Pons T, Dubertret B. Synthesis, encapsulation, purification and coupling of single quantum dots in phospholipid micelles for their use in cellular and in vivo imaging. Nat Protoc. 2007;2(10):2383-90.

107.	Seo HJ, Nam SH, Im HJ, Park JY, Lee JY, Yoo B, et al. Rapid Hepatobiliary Excretion of Micelle-Encapsulated/Radiolabeled Upconverting Nanoparticles as an Integrated Form. Sci Rep. 2015;5:15685.

108.	Renaud G, Hamilton RL, Havel RJ. Hepatic metabolism of colloidal gold-low-density lipoprotein complexes in the rat: evidence for bulk excretion of lysosomal contents into bile. Hepatology. 1989;9(3):380-92.

109.	Souris JS, Lee CH, Cheng SH, Chen CT, Yang CS, Ho JA, et al. Surface charge-mediated rapid hepatobiliary excretion of mesoporous silica nanoparticles. Biomaterials. 2010;31(21):5564-74.

110.	Heine M, Bartelt A, Bruns OT, Bargheer D, Giemsa A, Freund B, et al. The cell-type specific uptake of polymer-coated or micelle-embedded QDs and SPIOs does not provoke an acute pro-inflammatory response in the liver. Beilstein J Nanotechnol. 2014;5:1432-40.

111.	Pennycook SJ, Varela M, Hetherington CJ, Kirkland AIJMb. Materials advances through aberration-corrected electron microscopy. 2006;31(1):36-43.

112.	Levy M, Luciani N, Alloyeau D, Elgrabli D, Deveaux V, Pechoux C, et al. Long term in vivo biotransformation of iron oxide nanoparticles. Biomaterials. 2011;32(16):3988-99.

113.	Giustini AJ, Ivkov R, Hoopes PJ. Magnetic nanoparticle biodistribution following intratumoral administration. Nanotechnology. 2011;22(34):345101.

114.	Chertok B, Cole AJ, David AE, Yang VC. Comparison of electron spin resonance spectroscopy and inductively-coupled plasma optical emission spectroscopy for biodistribution analysis of iron-oxide nanoparticles. Mol Pharm. 2010;7(2):375-85.

115.	Zysler RD, Lima E, Jr., Vasquez Mansilla M, Troiani HE, Mojica Pisciotti ML, Gurman P, et al. A new quantitative method to determine the uptake of

SPIONs in animal tissue and its application to determine the quantity of nanoparticles in the liver and lung of Balb-c mice exposed to the SPIONs. J Biomed Nanotechnol. 2013;9(1):142-5.

116.   Zhang J, Ring HL, Hurley KR, Shao Q, Carlson CS, Idiyatullin D, et al. Quantification and biodistribution of iron oxide nanoparticles in the primary clearance organs of mice using T1 contrast for heating. Magn Reson Med. 2017;78(2):702-12.

117.   Crowe L, Wang Y, Gatehouse P, Tessier J, Waterton J, Robert P, et al., editors. Ex vivo MR imaging of atherosclerotic rabbit aorta labelled with USPIO— enhancement of iron loaded regions in UTE imaging. Proc Intl Soc Mag Reson Med; 2005.

118.   Wu LC, Zhang Y, Steinberg G, Qu H, Huang S, Cheng M, et al. A Review of Magnetic Particle Imaging and Perspectives on Neuroimaging. AJNR Am J Neuroradiol. 2019;40(2):206-12.

119.   Chakravarty R, Valdovinos HF, Chen F, Lewis CM, Ellison PA, Luo H, et al. Intrinsically germanium-69-labeled iron oxide nanoparticles: synthesis and in-vivo dual-modality PET/MR imaging. Adv Mater. 2014;26(30):5119-23.

120.   Freund B, Tromsdorf UI, Bruns OT, Heine M, Giemsa A, Bartelt A, et al. A simple and widely applicable method to 59Fe-radiolabel monodisperse superparamagnetic iron oxide nanoparticles for in vivo quantification studies. ACS Nano. 2012;6(8):7318-25.

121.   Pellico J, Ruiz-Cabello J, Saiz-Alia M, Del Rosario G, Caja S, Montoya M, et al. Fast synthesis and bioconjugation of (68) Ga core-doped extremely small iron oxide nanoparticles for PET/MR imaging. Contrast Media Mol Imaging. 2016;11(3):203-10.

122.   Shanehsazzadeh S, Oghabian MA, Daha FJ, Amanlou M, Allen BJJJoR, Chemistry N. Biodistribution of ultra small superparamagnetic iron oxide nanoparticles in BALB mice. 2013;295(2):1517-23.

123.   Kreyling WG, Abdelmonem AM, Ali Z, Alves F, Geiser M, Haberl N, et al. In vivo integrity of polymer-coated gold nanoparticles. Nat Nanotechnol. 2015;10(7):619-23.

124.   Rosebrough SF. Plasma stability and pharmacokinetics of radiolabeled deferoxamine-biotin derivatives. J Pharmacol Exp Ther. 1993;265(1):408-15.

125.   Wang H, Kumar R, Nagesha D, Duclos RI, Jr., Sridhar S, Gatley SJ. Integrity of (111)In-radiolabeled superparamagnetic iron oxide nanoparticles in the mouse. Nucl Med Biol. 2015;42(1):65-70.

126.   Arbab AS, Wilson LB, Ashari P, Jordan EK, Lewis BK, Frank JA. A model of lysosomal metabolism of dextran coated superparamagnetic iron oxide (SPIO) nanoparticles: implications for cellular magnetic resonance imaging. NMR Biomed. 2005;18(6):383-9.

127.   Lunov O, Syrovets T, Rocker C, Tron K, Nienhaus GU, Rasche V, et al. Lysosomal degradation of the carboxydextran shell of coated superparamagnetic iron oxide nanoparticles and the fate of professional phagocytes. Biomaterials. 2010;31(34):9015-22.

128.   Valdiglesias V, Kilic G, Costa C, Fernandez-Bertolez N, Pasaro E, Teixeira JP, et al. Effects of iron oxide nanoparticles: cytotoxicity, genotoxicity, developmental toxicity, and neurotoxicity. Environ Mol Mutagen. 2015;56(2):125-48.

129.   Gu L, Fang RH, Sailor MJ, Park JH. In vivo clearance and toxicity of monodisperse iron oxide nanocrystals. ACS Nano. 2012;6(6):4947-54.

130.   Park SH, Nam Y, Choi HS, Woo STJIMRI. Quantification of gadolinium concentration using GRE and UTE sequences. 2017;21(3):171-6.

131.   Bleicher AG, Kanal E. A serial dilution study of gadolinium-based MR imaging contrast agents. AJNR Am J Neuroradiol. 2008;29(4):668-73.

132.   Elster AD, Sobol WT, Hinson WH. Pseudolayering of Gd-DTPA in the urinary bladder. Radiology. 1990;174(2):379-81.

133.   Billotey C, Wilhelm C, Devaud M, Bacri JC, Bittoun J, Gazeau F. Cell internalization of anionic maghemite nanoparticles: quantitative effect on magnetic resonance imaging. Magn Reson Med. 2003;49(4):646-54.

134.   Kunzmann A, Andersson B, Thurnherr T, Krug H, Scheynius A, Fadeel B. Toxicology of engineered nanomaterials: focus on biocompatibility, biodistribution and biodegradation. Biochim Biophys Acta. 2011;1810(3):361-73.

135.   Liu M, Li Q, Liang L, Li J, Wang K, Li J, et al. Real-time visualization of clustering and intracellular transport of gold nanoparticles by correlative imaging. Nat Commun. 2017;8:15646.

136.   Aghighi M, Golovko D, Ansari C, Marina NM, Pisani L, Kurlander L, et al. Imaging Tumor Necrosis with Ferumoxytol. PLoS One. 2015;10(11):e0142665.

137.   Richter H, Kettering M, Wiekhorst F, Steinhoff U, Hilger I, Trahms L. Magnetorelaxometry for localization and quantification of magnetic nanoparticles for thermal ablation studies. Phys Med Biol. 2010;55(3):623-33.

138.   Hoopes PJ, Petryk AA, Gimi B, Giustini AJ, Weaver JB, Bischof J, et al. In Vivo Imaging and Quantification of Iron Oxide Nanoparticle Uptake and Biodistribution. Proc SPIE Int Soc Opt Eng. 2012;8317.

139.   Giustini AJ, Gottesman RE, Petryk AA, Rauwerdink AM, Hoopes PJ. Kinetics and pathogenesis of intracellular magnetic nanoparticle cytotoxicity. Proc SPIE Int Soc Opt Eng. 2011;7901.

140.   Pardoll DM. The blockade of immune checkpoints in cancer immunotherapy. Nat Rev Cancer. 2012;12(4):252-64.

141.   Gajewski TF, Woo SR, Zha Y, Spaapen R, Zheng Y, Corrales L, et al. Cancer immunotherapy strategies based on overcoming barriers within the tumor microenvironment. Curr Opin Immunol. 2013;25(2):268-76.

142.   Bonaventura P, Shekarian T, Alcazer V, Valladeau-Guilemond J, Valsesia-Wittmann S, Amigorena S, et al. Cold Tumors: A Therapeutic Challenge for Immunotherapy. Front Immunol. 2019;10:168.

143.   Korangath P, Barnett JD, Sharma A, Henderson ET, Stewart J, Yu SH, et al. Nanoparticle interactions with immune cells dominate tumor retention and induce T cell-mediated tumor suppression in models of breast cancer. Sci Adv. 2020;6(13):eaay1601.

144.   Feng Q, Liu Y, Huang J, Chen K, Huang J, Xiao K. Uptake, distribution, clearance, and toxicity of iron oxide nanoparticles with different sizes and coatings. Sci Rep. 2018;8(1):2082.

145.   Gatti-Mays ME, Balko JM, Gameiro SR, Bear HD, Prabhakaran S, Fukui J, et al. If we build it they will come: targeting the immune response to breast cancer. NPJ Breast Cancer. 2019;5:37.

146.   Aydin O, Chandran P, Lorsung RR, Cohen G, Burks SR, Frank JA. The Proteomic Effects of Pulsed Focused Ultrasound on Tumor Microenvironments of Murine Melanoma and Breast Cancer Models. Ultrasound Med Biol. 2019;45(12):3232-45.

국문 초록

가돌리늄 조영제의 독성에 대한 임상적 우려로 인해, 자기 공명 영상 (MRI)을 위한 새로운 조영제의 개발에 대한 관심이 증가하고 있다. 최근, 초소형 산화철 나노 입자 (ESIONs)는 생체 적합성 T1 조영제로서 상당한 주목을 받고 있다. ESIONs는 철 산화물 나노 입자 (IONPs)를 바탕으로 한 기존의 T2 조영제의 고유한 한계를 극복할 수 있다. 하지만 현재까지 ESIONs의 생체내 동태에 대한 연구는 제한적인 상태다. 향후 ESIONs의 임상적용을 위해서는 관련 연구가 필요한 상황이다.

본 연구에서, ESIONs은 비교적 높은 r1 이완도와 낮은 r2/r1 비를 보여 효율적인 T1 조영제로서의 가능성을 확인하였다. 실험실적 안정성 시험과 생체 내 안전성 시험을 바탕으로 64Cu의 방사능은 ESIONs의 생체 내 역학을 잘 반영한다는 것이 밝혀졌다. 방사성 표지 된 ESIONs을 이용하여 생체 내 분포 및 약동학을 평가한 결과, ESIONs는 비교적 긴 시간 혈액 내 분포하였으며 간담도를 통해 빠르게 배설되는 것을 확인하였다.

또한, PET/MRI를 사용하여, PET 유래 방사능의 동적 변화 및 MRI 신호 강도를 동일한 시점에서 직접 비교 평가하였다. PET 및 MRI 신호의 불일치는 고농도 범위의 ESIONs가 투여되는 경우나 ESIONs가 세포 내로 함입되는 경우 발생함을 밝혔다.

비교적 긴 혈액 순환 시간과 간담도계를 통한 빠른 배설을 바탕으로 ESION은 혈액 풀 영상 조영제로서 높은 효율성과 안전성을 동시에 가질 것으로 기대된다. 또한, 방사능 표지 ESION은 서로의 강점과 약점을 보완함으로써 다양한 임상 상황에서 적용 가능할 것으로

기대된다.

주요어 : 산화철 나노 입자, 초소형 산화철 나노 입자, 양전자 단층 촬영, 자기 공명 영상

학번: 2016−30724